Scholars' Mine

Summer 2018

Modeling and control of three-phase grid-connected PV inverters in the presence of grid faults

Paresh Vinubhai Patel

Recommended Citation

MODELING AND CONTROL OF THREE-PHASE GRID-CONNECTED PV

INVERTERS IN THE PRESENCE OF GRID FAULTS

by

PARESH VINUBHAI PATEL

A THESIS

Presented to the Graduate Faculty of the

MISSOURI UNIVERSITY OF SCIENCE AND TECHNOLOGY

In Partial Fulfillment of the Requirements for the Degree

MASTER OF SCIENCE

in

ELECTRICAL ENGINEERING

2018

Approved by

Dr. Jonathan Kimball, Advisor
Dr. Mehdi Ferdowsi
Dr. Pourya Shamsi

ABSTRACT

A two-stage photovoltaic grid-connected microgrid modeling approach is presented in this work. The purpose of the modeling is the behavior study of the microgrid during the low-voltage event on the grid. A complete mathematical model is discussed for each component of the system. The MPPT of the photovoltaic system is integrated with the boost controller to inject the constant current in the DC-link. The boost converter and the inverter control is implemented using the cascaded PI control. A dual second-order generalized integrator (DSOGI) method is implemented for the sequence extraction. The inverter controller is designed to meet the grid-code requirement of low-voltage ride through (LVRT) and reactive power injection. The simulation model is designed in a MATLAB/PLECS environment, and the controller design is validated by running a low-voltage event on the grid.

To observe the interaction of a multiple PV system with the grid, a nonlinear average model of the two-stage grid-connected PV system was designed and validated against the switching model. A low voltage event on the grid was simulated to observe the impact on the multiple PV system. A power quality event of voltage dip during the unbalance voltage on the grid is presented. The implication of the ungrounded system during the low-voltage event is explained. In addition, the importance of grounding and the effect of the line impedance for the why-connected system is described in detail.

ACKNOWLEDGMENTS

I would like to thank my advisor, Dr. Kimball for giving me the opportunity to work on this project. Thank you for all your patience and for helping me build on the basic and advance concepts on this topic. I am grateful for your direction throughout the course of my research work.

I am thankful to Dr. Ferdowsi and Dr. Shamsi for serving committee members and taking time to review my work.

I would like to thank Vikram Chowdhury for his timely support at various stages of this project. Also, thanks to Dr. Jacob Mueller for his interest and help. I am also grateful to my friend and lab mate Prateek for his encouragement and valuable advice in my thesis completion. Thanks to all my friends and family members who always showered me with their support and help.

Lastly, I would like to thank my mother and father, without whom I can't imagine any endeavor in my life. I am so grateful to you that my words can't describe the strength I received from you over the years.

TABLE OF CONTENTS

LIST OF ILLUSTRATIONS

LIST OF TABLES

1. INTRODUCTION

The consumption of electric power is increasing with the growing population all over the world, and it is a challenging situation for countries to supply the increased load demand with the traditional methods of power generation and distribution. The major challenges are the planning horizon and the economy. Extensive planning is required to build large power plants, and it is a time-consuming process. Moreover, to supply the scatter load or distant load, such planning may not be economical because it is very capital intensive. New methods of power distribution are in sheer demand, which can overcome the above-mentioned challenges if proper planning is carried out [1]. Also, future power system development should consider the impact on the environment and the economy. Above factors should be considered for future power generation and it should be reliable, economical, safe, and feasible.

Nowadays, various distributed energy resources (DER) such as photovoltaic (PV) and wind energy production are increasing because of cost reduction, availability of the resources, and the advanced research conducted in this area. However, the nature of these resources is intermittent, which eventually reduces the efficiency of an independent resource [2]. For example, during low sun hours, the output from PV falls significantly so that it cannot serve the load requirement. Also, wind generator production faces a similar problem due to its dependency on the wind velocity, which is a variable factor. The overall performance of distributed energy resources (DER) can be improved by integration with the utility grid [2]. This can be achieved using a microgrid which acts as the integrating network of a various DER and the grid. The microgrid can offer higher reliability, power quality, reduced carbon emissions, and a cost-competitive solution over the traditional power distribution system. Thus, numerous studies are carried out to analyze the fitness of the microgrid at low and medium voltage levels. The different energy sources that fall

under DER category are PV, wind generators, fuel cells, micro-turbines, combined heat and power (CHP) units, and energy storage devices such as a battery. Most of the DER will be connected to the grid using an inverter as the interfacing medium, which necessitates the better understanding of the inverter.

In recent years, PV production has increased and its influence on the power system is drawing more attention. The typical PV system is comprised of PV arrays, maximum power point tracker (MPPT), boost controller, and the inverter as the interfacing medium with the grid. Due to changing environmental conditions, the operating point of the PV array changes, which affects the output power of the PV array. Thus, the overall efficiency of the operation will be reduced. Using MPPT, one can ensure the maximum output power, which adapts to changes in the irradiation level and the temperature. The boost converter serves the purpose of voltage regulation along with the voltage boost which is required to isolate the AC part from the PV side. The inverter is used as an interfacing medium to the grid, which can be directly used to serve the load. Though the addition of each of these components adds cost to the overall system, the power quality and operation performance improves [3]. Therefore, the cost can be justified for each integrated piece of equipment in a PV system. Due to the continuous improvement in power electronics devices and cost reduction of PV technology, the typical PV system will house all the above-mentioned equipment.

In a traditional power distribution system, the utility company is responsible for maintaining the power quality on the consumer end. Therefore, the utility companies have been constantly improving the control strategy and other measures to guarantee high power quality to the consumer [4]. The penetration of renewable energy into the distribution system at a medium and low-voltage level poses various challenges to maintaining the power quality and operation integrity, due to the independent operation of the distributed generation (DG). Moreover, the voltage sag events are an additional burden on the utility companies. Thus, the grid regulations such as anti-islanding and low-voltage ride through

(LVRT) are imposed on the PV system to ensure the desired control during unbalanced conditions [5, 6]. It will help in the coordination of traditional and renewable energy resources, which eventually improve the grid control. The LVRT grid code dictates that the microgrid should remain connected for a certain time to support the grid. In addition, it should supply some reactive power based on the voltage sag at the point of common coupling (PCC). The above grid regulations can be met using the inverter grid control thus, the study of inverter control is crucial for grid requirements compliance [7].

The balanced and the unbalanced faults are the root cause for the grid-regulation necessity due to the severity of the effects caused on the grid and the microgrid. As explained earlier, the power quality should remain intact, which can be affected by the unbalanced event on the grid. The possibility of the unbalanced event on the microgrid is very low compared to the disturbances on the grid side. During the unbalanced event on the grid, a high current flow from the microgrid to the grid and it can damage the microgrid equipment. Moreover, the unbalanced fault situation causes active power oscillations, which will be reflected on the DC-link. The total harmonic distortion (THD) will also increase during an unbalance fault situation [8]. Thus, it is extremely important to identify such events and take proper action to minimize the damage to the microgrid and cause less harm to the interconnected loads and grid. The inverter control can be designed to limit the current and reduce the active power oscillations during a fault.

The conventional method of the inverter control contains the outer power loop and the inner current control loop [9]. The purpose of the outer loop is to track the power flow through the inverter, which generates the specific current reference for the inner current loop. This current reference will be compared against the actual inductor current flowing past the inverter through the LCL filter. It generates the error signal, which will be added with the coupling terms to produce the gating signal for the inverter [10]. The disadvantage of the traditional converter method is a failure to fulfill the grid requirements and increase the power quality issues during disturbances. Since the unbalance in the system causes

generation of the negative sequence component that plays a key role in most of the issues during a fault, it is necessary to perform the sequence extraction for a voltage as well as a current. The next step should be an individual current control based on the requirement of the inverter design.

To achieve it, one should have the current reference generation (CRG) for positive and negative sequence currents to be controlled. Various CRG methods are reviewed here that are frequently used for the grid-connected inverter [11]. The instantaneous active reactive control (IARC) method incorporates the three-phase voltage control and does not extract the positive and negative sequence of the voltage. The disadvantage of this method is the injection of a non-sinusoidal current during a fault along with a high THD injection. To overcome the limitation of IARC, the active and reactive control (AARC) method, which uses the average value of the voltage for the current generation is proposed, but this method generates double the grid frequency oscillations of the active power. To avoid the active power oscillations, the positive and negatives sequence control (PNSC) method is presented which has double the grid frequency oscillations of active and reactive power. The balanced positive sequence control (BPSC) method is introduced, which uses positive sequence voltage control for the current reference generation to inject the balanced current into the grid. All the methods discussed so far have the downfall of active and reactive power oscillation or injection of a non-sinusoidal current during a fault. In consideration of the above facts, a dual current controller method is proposed in this work. It implements the dual second order generalized integrator (DSOGI) method for the sequence extraction for the voltage and the current. The current reference generation is performed based on the design requirement that focuses on the current limitation and the DC-link voltage oscillation reduction. The efficacy of the proposed controller for a single PV system is validated using the simulation in MATLAB/PLECS environment.

In the near future, the penetration of the PV system will increase at the distribution level, which inspires the study of the multiple PV grid-connected system. The indirect application of this study is behavior analysis of multiple grid-connected PV inverter systems. The current challenges in multiple inverter systems are power sharing, stability due to the resonance, and protection issues [12]. The purpose of the multiple PV study is to learn the system stability and power quality issues during a low voltage event. The absence of the grounding will result in the protection failure at mid-voltage and high-voltage levels but it might be overlooked at low-voltage level. The reason for the negligence could be over-current protection of equipment and low touch potential voltage. Thus, the grounding issue is exploited here to study the impacts during faults. Since the switching model has a longer simulation time, a nonlinear average model of the complete system is designed and then the single line-to-ground (SLG) fault is run to observe the effects of a low-voltage event on the microgrid. The effects of the line impedance and the consequences of the ungrounded system are also explored.

The outline of the thesis is as follows. First, the review and the modeling of the two-stage three-phase grid-connected PV system is performed. Then, the fault analysis and its impact study on the PV system is explained in detail. The simulation results are presented to prove the efficacy of the proposed controller during the normal as well as fault condition. Then, the nonlinear average modeling for the complete two-stage grid-connected system is explained. Finally, the multiple PV system is designed and the fault event is run to observe the effect of an ungrounded system during a low-voltage event.

6

2. MODELING OF TWO-STAGE THREE-PHASE GRID-CONNECTED PV SYSTEM

A two-stage grid-connected PV inverter consists of separate modular blocks that collectively form the grid-connected system of PV generation. These modular blocks can differ based on the purpose of a study and its complexity. The different blocks used for the current research are PV arrays, a boost controller, an inverter, an LCL filter, a load and the grid. The combination of these blocks is shown in Figure 2.1, which formulates the common but complex system desired for the current research work. First, the basic review for each block is presented in brief to set the base for the design. Then, the comprehensive modeling practice of each block is explained. Finally, the entire two-stage three-phase grid-connected switching model is presented in a MATLAB/PLECS environment.

The system under consideration is presented in Figure 2.2, which represents the schematic diagram of the three-phase grid-connected PV system. It is the two-stage structure of the PV system, namely DC-DC conversion and DC-AC conversion. The output from the solar PV is connected to the boost converter, which has two functions: (1) Extract the maximum power from the PV source (2) Boost and regulate the DC output voltage from PV. The next stage is the DC-AC conversion, which takes the DC input from the boost converter and injects the AC power into the grid. In between the inverter and the grid, an LCL filter
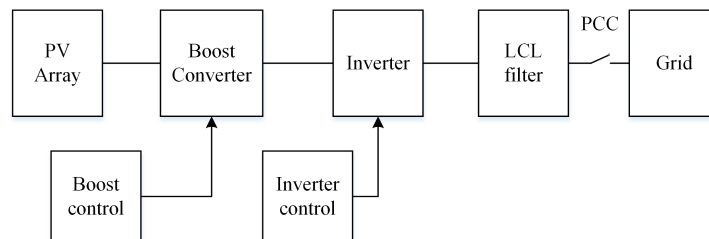
Figure 2.1. Block diagram of a grid-connected PV system
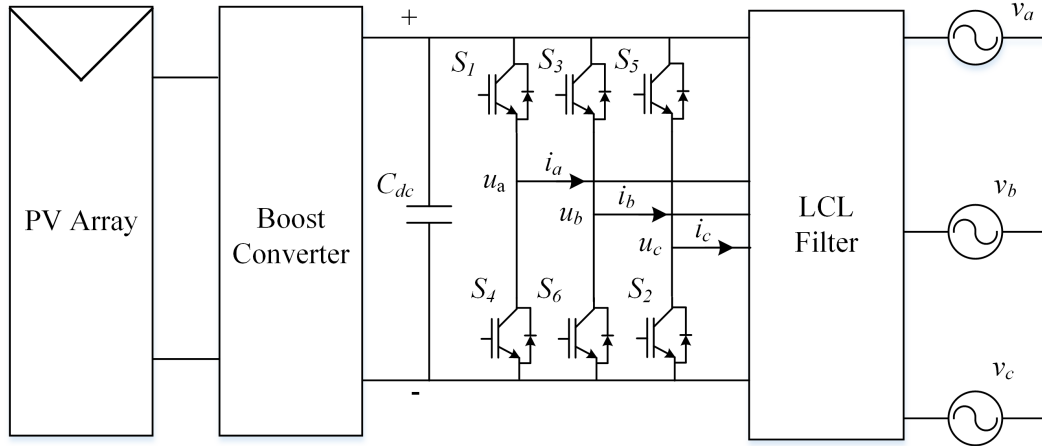
Figure 2.2. Two-stage three-phase PV system configuration

is connected to eliminate the higher frequency harmonics from the inverter output. The description of the various parameters is as follows: V_{dc} indicates the DC input voltage to the inverter; C_{dc} is the capacitance for maintaining the constant DC input voltage to the inverter also called as DC-link; u_a, u_b, and u_c respectively represents the output per-phase voltages of the inverter; i_a, i_b, and i_c are the three-phase output current from the grid-connected inverter; v_a, v_b, and v_c stand for the grid phase voltages respectively, and the LCL block represents the filter connected between the grid and the inverter. The simulation results describing the steady-state behavior of the model is presented at the end of the section to verify the accuracy of the proposed model. The remainder of this section describes each block of the system separately.

2.1. PV ARRAY MODELING

A solar cell is basically a p-n junction diode that generates the charge carriers when an incident photon has energy greater than the bandgap of the semiconductor component element. Nowadays, various polycrystalline solar cells are available along with the tradi-
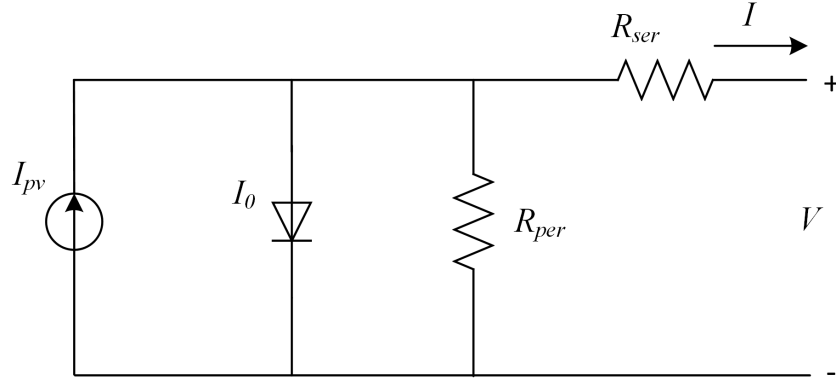
Figure 2.3. Single cell PV equivalent circuit

tional monocrystalline solar cell. Solar cell characteristics are unideal and much research work has been carried out to obtain the solar equations that best fit the behavior in practical conditions. The basic ideal model is represented by a current source in parallel with a diode.

As shown in Figure 2.3, the current source represents the current generated by the photovoltaic cell, and the diode indicates the Shockley diode. The total current generated by a solar cell is the net current from the current source and the diode [13]. The ideal solar model is amended by the addition of a series and parallel resistance, which are shown in Figure 2.3.

The basic equation of a single solar cell is

$$I = I_{pv} - I_0 \left[e^{(qV/akT)} - 1 \right] \tag{2.1}$$

here I represents the net current from a single solar cell; I_{pv} is the total current generated by a solar irradiation; I_0 indicates the reverse saturation current (leakage current) of a diode; a is the ideality factor of a diode, which represents the adjustment required to meet the theoretical PN junction characteristics of a solar cell to the measured values; T is the temperature of a diode in Kelvin; q is the charge of an electron $1.602\,176\,46 \times 10^{-19}$ C; and k is the Boltzmann constant having value of $1.380\,650\,3 \times 10^{-23}$ J/K.

Equation (2.1) is inadequate to describe the characteristics of a practical solar cell. The inclusion of a series and parallel resistance along with the observation of the terminal voltage makes the model best fit for the empirical conditions.

$$I = I_{pv} - I_0 \left[\exp\left(\frac{V + R_{ser}I}{V_t a} \right) - 1 \right] - \frac{V + R_{ser}I}{R_{per}} \tag{2.2}$$

here R_{ser} indicates the total series resistance of all the solar cells; R_{per} indicates the equivalent parallel resistance of solar cells; V_t is the thermal voltage which can be calculated as $V_t = kT/q$; V is the terminal voltage of combination of solar cells; and R_{ser} exists due to the contact resistance between the solar cell and the connection terminal, whereas R_{per} originates from the leakage current of the p-n junction. Equation (2.2) can be changed according to the number of series and parallel combinations of solar cells used in PV array. Increasing the series cell will raise the voltage while increasing the parallel cells will increase the current level of a PV array.

The amount of light-generated current depends on the generated charges due to the sunlight irradiation and temperature as shown in (2.3)

$$I_{pv} = (I_{pvn} + K_i \Delta T) \frac{G}{G_n} \tag{2.3}$$

It is assumed that the short circuit current is approximately equal to the nominal photovoltaic current because the value of series resistance would be very low compared to the parallel resistance of the solar cell. In Equation (2.3), I_{pvn} is the nominal photovoltaic current generated (in A), k_i is the current coefficient, ΔT (in K) is the difference of T (actual temperature) and T_n (nominal temperature), G is the incident solar radiation, and G_n is the nominal solar radiation. Both G and G_n are given in W/m^2.
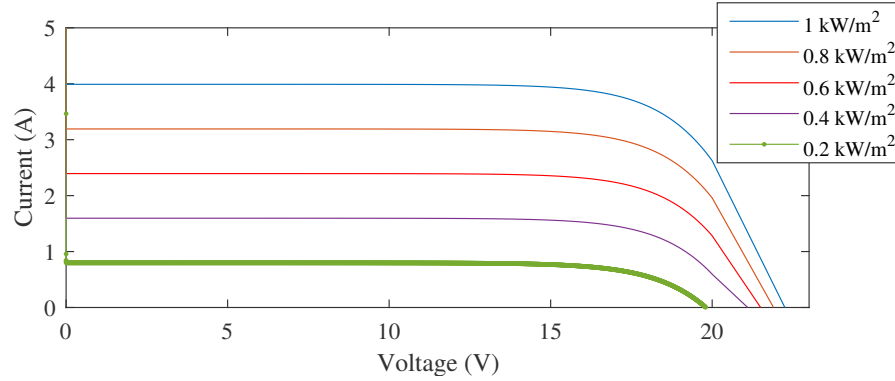
Figure 2.4. Single solar cell IV characteristics
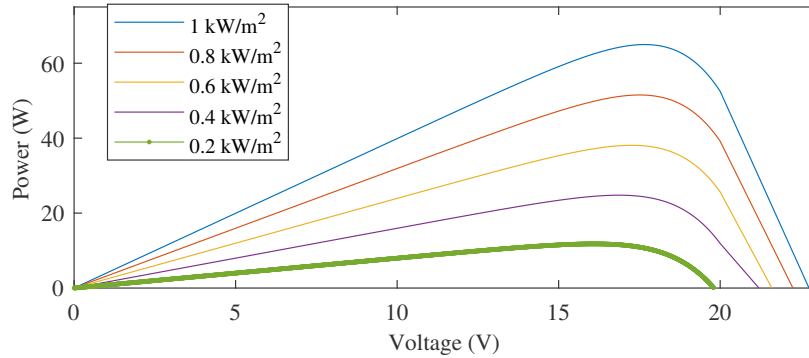
Figure 2.5. Single solar cell PV characteristics

Various formulae are available to match the design characteristics of the solar cell. The formula that best matches the solar cell properties of high open circuit voltage and large temperature variation can be given by

$$I_{on} = \frac{I_{scn} + K_i \Delta T}{\exp((V_{ocn} + K_v \Delta T)/aV_t) - 1} \tag{2.4}$$

In Equation (2.4), V_{ocn} is the nominal open-circuit voltage, K_v is the voltage coefficient, I_{scn} is the nominal short-circuit current (in A), and a and V_t are ideality factor and thermal voltage respectively. The combination of (2.2), (2.3), and (2.4) can be used to model the solar cell which can vary output based on irradiation level and temperature conditions. All the

equations mentioned before are useful in PV modeling, which can have the characteristics to the practical PV array. Since the purpose of the study is to focus on the inverter control design, the PV model is used from three-phase grid-connected inverter model (PLECS) having the solar cell characteristics presented in Table 2.1. A single PV module contains 20 series and 2 parallel cells. Two such PV modules are connected in parallel. A combination of the above-mentioned configuration is connected in series with the same combination to form a complete PV array. The PV and IV curve for the BP365 solar cell is presented in Figure 2.4 and Figure 2.5.

Table 2.1. BP365 solar cell characteristics

Maximum power (Pmax)	65 W
Voltage at Pmax	17.6 V
Current at Pmax	3.69 A
Short-circuit current (Isc)	3.99 A
Open-circuit voltage (Voc)	22.1 V
Temperature coefficient of Isc	$(0.065\pm0.015)\%/°C$
Temperature coefficient of Voc	$-(80\pm10)mV/°C$
Temperature coefficient of power	$-(0.5\pm0.05)\%/°C$

2.2. MAXIMUM POWER POINT TRACKING

In solar generation, it is of utmost important to maximize the power output from a solar panel. A solar cell has non-linear behavior and hence cannot generate a constant power. Moreover, ambient conditions like irradiation level and the temperature keeps changing, which changes the power characteristics of the solar cell. To obtain maximum power, the output voltage of a solar cell should be tracked such that it will be close to the maximum power point at different irradiation and temperature conditions. By means of MPPT, the overall efficiency of a solar cell can be increased since maximum power will be extracted
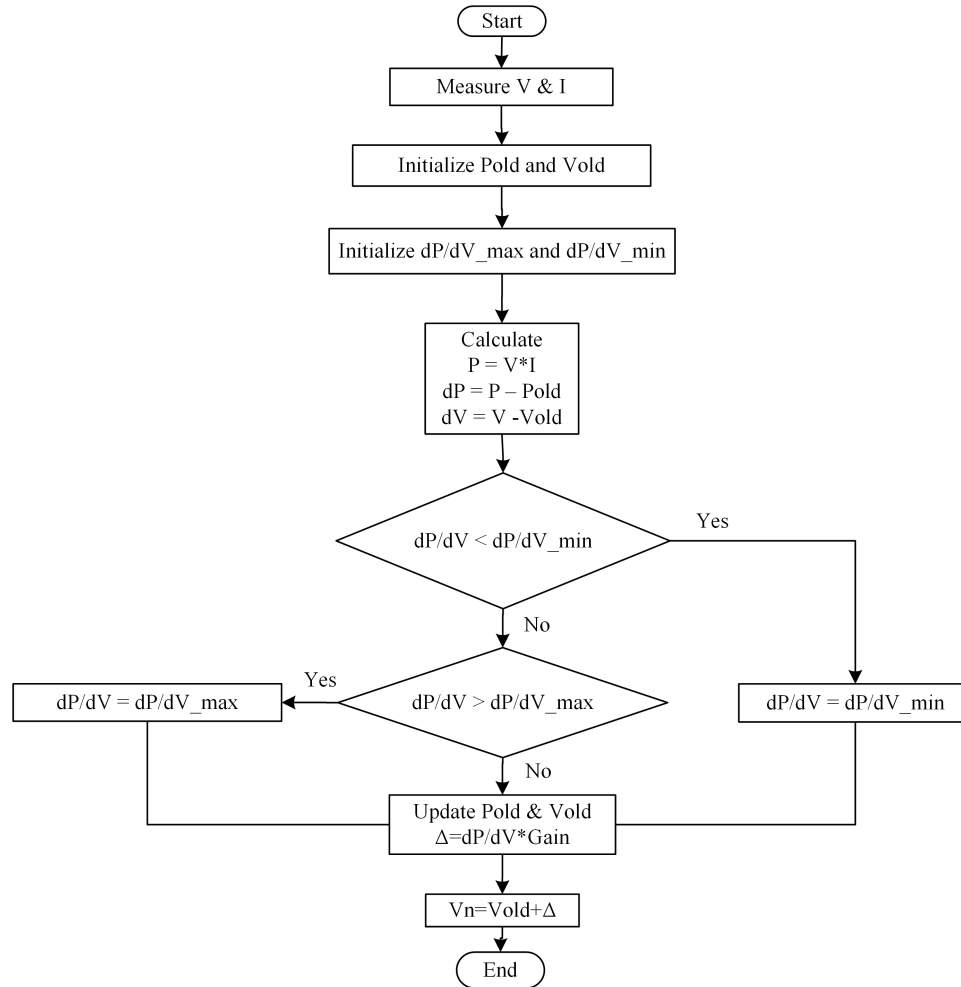
Figure 2.6. MPPT algorithm

from the PV array during normal daylight hours. MPPT algorithms are gaining popularity because of the high efficacy and improved version to extract the maximum power from the solar cell.

Many different algorithms are available for MPPT controller. The most common are perturbation and observation (P&O), incremental conductance method (IC), and fuzzy logic controller method. The methods mentioned above differ in complexity, stability, and speed [14]. The designer will select the method based on the design requirement of the system. In this work, a fuzzy logic controller, also called the dP/dV method is selected. This

method is more effective in tracking the irradiation changes and less complex compared to other methods. Also, it does not oscillate at MPP point like the P&O method. The fuzzy logic control method deploys the logical control based on the nested loops, which adds automation in the process. Though this method is relatively slower compared to other methods, it is used due to its stable steady-state and fewer oscillations at MPP.

The dP/dV method deployed here uses the principle of a maxima. According to the dP/dV theorem, the maximum value of a function can be found using the knowledge of a derivative of the function.The point at which the derivative of the function would be zero, the corresponding parameter of the function will give the maximum value of the function. For obtaining maximum power that is the function of a voltage and a current, dP/dV is used, which is nothing but the slope of the PV curve. When the value of dP/dV becomes zero, the maximum voltage for the MPP point can be obtained. Figure 2.6 represents the algorithm for dP/dV tracking. The tracked dP/dV value is multiplied with sampling term to obtain the error signal. This error will be added to the previous sample value voltage reference. At MPP, when dP/dV reaches zero value, the reference voltage settles to the maximum power point and maintains that constant voltage until the external condition or any disturbance is present in the system.

2.3. BOOST CONVERTER AND CONTROLLER DESIGN

A boost converter is used widely in renewable energy application such as solar generation and wind generation. Because of intermittency of solar and wind generation, it is very important to make the overall system efficient to counterbalance the effect of intermittency. A boost converter contributes towards improvement in efficiency of an overall system. A boost converter converts a low-voltage level to a high-voltage level. In addition, it regulates the power extracted from PV array along with the constant voltage application at the terminal output.
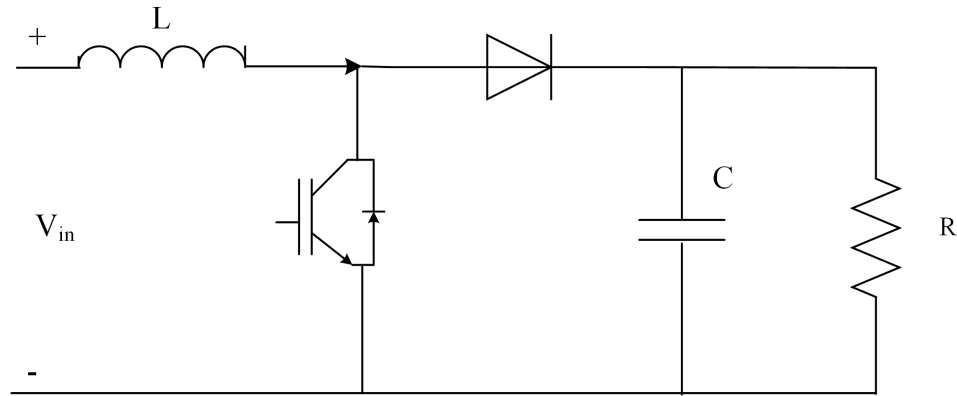
Figure 2.7. Boost converter configuration

The two-stage PV array connected to the grid will require a constant current injection in the DC-link, which is the output capacitor of the boost converter. A constant current injection will ensure the constant voltage of the DC-link and limited fluctuation in the output voltage variation. Hence, the inverter will get the constant input DC voltage, which is necessary to improve the performance and efficiency of an inverter. Moreover, the cost of a boost converter is less compared to the other converters. Figure 2.7 represents a basic illustration of a boost converter having input voltage V_{in} and output voltage V_o. During on switching, the diode will be reversed biased, and hence input current would be same as the inductor current. The output voltage during the on-interval would be the voltage across the capacitor. The value of the capacitor should be sufficiently large enough to maintain the constant voltage across the load. During the off-interval, the inductor will discharge in the reverse direction, which will cause a diode to become forward biased. The voltage across the inductor would be the difference between the input voltage and output voltage. The relation between the input voltage and output voltage can be derived using the volt-sec balance across the inductor. According to the volt-sec balance, the steady-state voltage across the inductor would be zero for one cycle. The relation between the output voltage

and the input voltage is given below:

$$V_o = \frac{V_{in}}{(1 - D)} \tag{2.5}$$

here $D = T_{on}/T_{switch}$ is the duty ratio of the on-time interval over the switching time T, V_{in} is the input voltage, and V_o is the output voltage of a boost converter. Similarly, the relation between the output current I_o and the input current I_{in} can be obtained assuming zero losses in the circuit, as shown in (2.6)

$$I_o = I_{in}(1 - D) \tag{2.6}$$

The boost converter can be designed in either continuous conduction mode (CCM) or discontinuous conduction mode (DCM). In CCM, the inductor current will be a non-zero value, whereas in DCM, the inductor current attains zero value and may have interleaved timing of zero inductor current for time Δt.

The two main factors for the boost converter design are the inductor and capacitor selection. The values of an inductor and a capacitor are finalized based on several factors. The main equation that governs the selection of an inductor for the boost converter design is

$$L = \frac{D(1 - D)V_{dc}}{f_{sw}\Delta I_L} \tag{2.7}$$

here D is the duty cycle of the boost converter, V_{dc} is the DC-link voltage, f_{sw} is the switching frequency of the boost converter, and ΔI_L is the inductor current ripple [15]. The value of L is selected considering the maximum value of ΔI_L possible. The inductor selection is performed based on (2.7). The D value turns out to be 0.125 for the input voltage of 700 V from (2.7). The desired ΔI_L is 30% for the switching frequency of 50 kHz and the output voltage of 800 V. Thus, an inductor value of 5 mH is selected for the boost converter.

The selection of the capacitor is a very critical factor in regards to the overall performance of the boost converter. It should be sufficiently large to reduce the power oscillation towards the grid, and if not, then it may cause oscillation in the active and

reactive power towards the grid. In addition, it should limit the voltage ripples of the DC-link to increase the life of an inverter. Equation (2.8) governs the selection of a capacitor value for the boost converter;

$$C_{dc} = \frac{P_{in}}{\omega V_{dc} \Delta v_{dc}} \tag{2.8}$$

here P_{in} is the power injected into the grid, Δv_{dc} is the voltage ripple, and ω is the angular frequency in radians per seconds. The selected voltage variation guarantees the minimal effects on the total life of the DC-link. To select the DC-link capacitance, a maximum power injection capability of 10.4 kW is considered. The voltage ripple Δv_{dc} of 0.5 V is considered to have an output voltage of 800 V. Using (2.8), an approximate value of 50 mF is selected.

The typical boost control design contains a single closed loop control of the boost controller. These controllers may control the voltage or power through the boost controller. The resultant error from the controller will drive the PWM, which changes the duty ratio of the boost converter. The major disadvantage of the conventional single-loop boost controller is the uncontrollability of the current flowing through the boost converter. The current control is desired to inject the constant current into the inverter with less ripple. It can be achieved using the dual loop control, which contains an outer voltage loop and inner current control loop. In addition, the transfer function of the boost converter has zeros in the right half plane and a phase margin greater than 180°. Therefore, the conventional voltage control method would not be sufficient for the boost control. The outer voltage loop here controls the constant PV terminal voltage, which generates the reference signal for the inner current loop. The error single from the inner current control loop drives the PWM of the boost converter.

Figure 2.8 shows the schematic of the outer PV voltage controller and the inner current controller. The reference voltage for the outer voltage loop is set by the MPPT output. This ensures that the voltage will be maintained at the maximum output voltage from the PV. The error signal from the outer loop generates the current signal, which
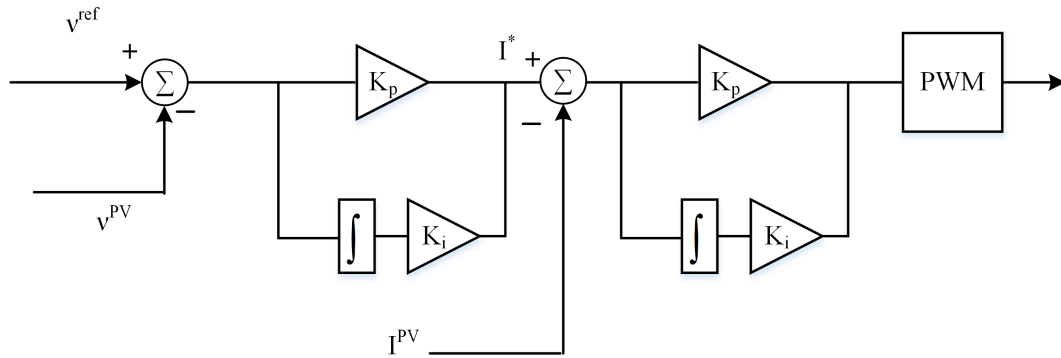
Figure 2.8. Boost controller loop

becomes the reference for the inner control loop. The MPPT sets the reference voltage to approximately 704 V, which can be verified from PV curve of the single solar cell. The generated reference current from the outer loop is compared with the PV output current which controls the duty ratio of the PWM for the boost converter. This cascaded control process of the boost control injects the constant current into the inverter and controls the duty ratio accordingly.

2.4. AC SYSTEM DESIGN

The equations for the three-phase balanced grid can be represented by:

$$
\begin{aligned}
v_a &= V\cos(\omega t) \\
v_b &= V\cos(\omega t - 2\pi/3) \\
v_c &= V\cos(\omega t + 2\pi/3)
\end{aligned}
\tag{2.9}
$$

These equations represent the three-phase grid voltages having peak voltage V and angular frequency ω. The equations that depict the relation between the grid and the inverter can be represented as follows [16]:

$$
\begin{pmatrix} \frac{di_a}{dt} \\ \frac{di_b}{dt} \\ \frac{di_c}{dt} \end{pmatrix} = \begin{pmatrix} \frac{-R}{L} & 0 & 0 \\ 0 & \frac{-R}{L} & 0 \\ 0 & 0 & \frac{-R}{L} \end{pmatrix} \begin{pmatrix} i_a \\ i_b \\ i_c \end{pmatrix} + \frac{1}{L} \begin{pmatrix} u_a - v_a \\ u_b - v_b \\ u_c - v_c \end{pmatrix}
\tag{2.10}
$$

Equation (2.10) is presented in a three phase abc reference frame. After performing the transformation method, the above equations can be represented in synchronous rotating reference frame as shown in (2.11):

$$
\begin{pmatrix} \frac{di_d}{dt} \\ \frac{di_q}{dt} \end{pmatrix} = \frac{1}{L} \begin{pmatrix} -R & \omega L \\ -\omega L & -R \end{pmatrix} \begin{pmatrix} i_d \\ i_q \end{pmatrix} - \frac{1}{L} \begin{pmatrix} v_d \\ v_q \end{pmatrix} + \frac{1}{L} \begin{pmatrix} u_d \\ u_q \end{pmatrix}
\tag{2.11}
$$

As presented in (2.11), i_d and i_q are the d-axis and q-axis component of the output current of the inverter, u_d and u_q represent the d-axis and q-axis component of inverter output, v_d and v_q are d-axis and q-axis components of the grid voltages respectively.

$$
u_d = L\frac{di_d}{dt} + Ri_d - \omega Li_q + v_d
$$
$$
u_q = L\frac{di_q}{dt} + Ri_q + \omega Li_d + v_q
\tag{2.12}
$$

The simplified equations of the inverter voltage in the synchronous rotating frame are presented in (2.12) which describe inverter output as the sum of the grid voltage and other coupling components. Equation (2.12) indicate the coupling of d and q axis control. For making the system stable in closed-loop control, PI regulator is used in addition to the decoupling control using feedforward voltage as presented in (2.13).

$$
u_d = (K_p + \frac{K_i}{s})(i_d^* - i_d) - \omega Li_q + v_d
$$
$$
u_q = (K_p + \frac{K_i}{s})(i_q^* - i_q) + \omega Li_d + v_q
\tag{2.13}
$$

The LCL filter is used to remove the higher order switching harmonics from the input signal. The parameters of the LCL filter are presented in Table 3.4.

2.4.1. Active and Reactive Power Equations. The instantaneous active and reactive power of three-phase grid-connected inverter can be realized using d-axis and q-axis voltages and currents using following equations:

$$P = \tfrac{3}{2}(v_d i_d + v_q i_q)$$
$$Q = \tfrac{3}{2}(v_q i_d - v_d i_q)$$

(2.14)

The separate control of the active and reactive power can be achieved by realizing either v_d or v_q equals to zero. If $v_d = 0$, then Equation (2.14) will result into the independent control of the active power and reactive power using d-axis and q-axis current control as presented in (2.15).

$$P = \tfrac{3}{2} v_d i_d$$
$$Q = -\tfrac{3}{2} v_d i_q$$

(2.15)

2.4.2. Reference Frame Transformation. The voltage and current control are required to obtain the control flow of the active and reactive power. Controlling three-phase in the stationary reference frame is very challenging because it involves different phases separated by $120°$. The process of the reference frame transformation reduces the number of the phases involved in the control process, which improves the control methods by reducing the challenges involved with the three-phase control. The two most common reference frame transformations are $\alpha\beta$ (stationary reference frame) and dq (rotating reference frame) transformations.

The reference frame transformation can be accomplished using Clarke (stationary reference frame) and Park transformation (rotating reference frame). Equation (2.16) and (2.17) represent the conversion equations from abc to $\alpha\beta$, and $\alpha\beta$ to dq reference frame,

$$V_\alpha = \frac{2}{3}\left(V_a - \frac{V_b}{2} - \frac{V_c}{2}\right)$$

$$V_\beta = \frac{1}{\sqrt{3}}(V_c - V_b)$$
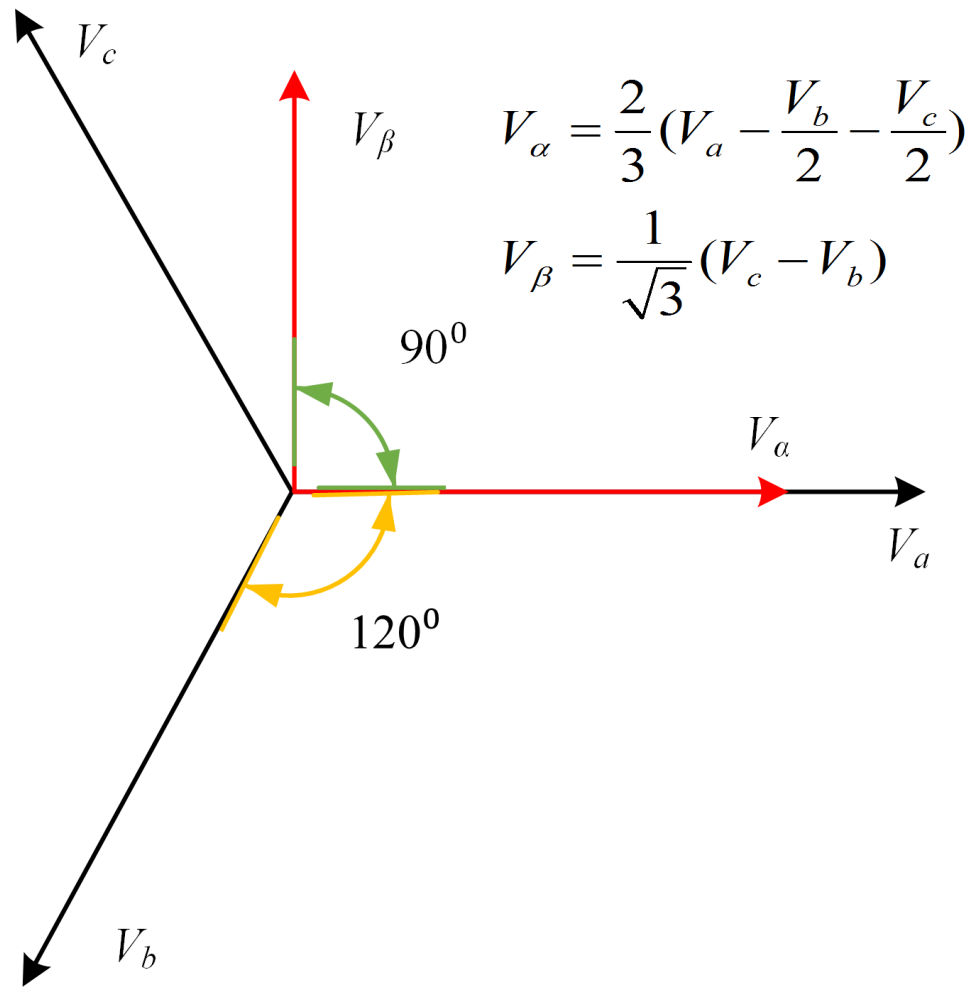
Figure 2.9. abc to stationary reference frame $(\alpha\beta)$ conversion

respectively.

$$\begin{pmatrix} V_\alpha \\ V_\beta \end{pmatrix} = \frac{2}{3}\begin{pmatrix} 1 & -1/2 & -1/2 \\ 0 & -\sqrt{3}/2 & \sqrt{3}/2 \end{pmatrix}\begin{pmatrix} V_a \\ V_b \\ V_c \end{pmatrix} \tag{2.16}$$

$$\begin{pmatrix} V_d \\ V_q \end{pmatrix} = \begin{pmatrix} \sin\theta & \cos\theta \\ \cos\theta & -\sin\theta \end{pmatrix}\begin{pmatrix} V_\alpha \\ V_\beta \end{pmatrix} \tag{2.17}$$
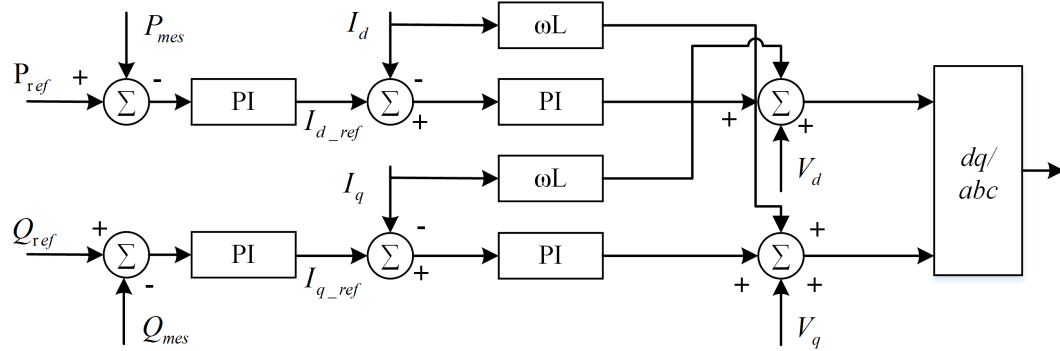
Figure 2.10. Inverter conventional current controller

The stationary reference frame transformation implemented in this work is presented in Figure 2.9. As indicated in Figure 2.9, V_α is aligned with a phase, whereas V_β leads by 90°. Next, the synchronous reference frame transformation is performed on the stationary voltage using (2.17). The conversion process has the position of V_d and V_q interchanged with the conventional abc to dq transformation.

      2.4.3. Inverter Control Design. For microgrids, both voltage source inverter (VSI) and current source inverter (CSI) are commonly used. Also, the selection of the control strategy depends on the mode of operation. For example, during islanded operation, the most prominent control strategy used is the droop control. The advantage of the droop control is allowing variation in the voltage and frequency based on the load variation. For the grid-connected mode, the microgrid follows the voltage and frequency of the grid, and it needs to supply power based on the commanded power from the central controller or maintain certain power based on the capability of the microgrid. Thus, the power control is a crucial factor for the grid-connected inverters. In addition, it is also equally important to regulate the current injected into the grid from the power quality and protection perspectives. To fulfill these requirements, the inverters selected are current controlled VSI. This common grid-connected inverter control system contains the outer power loop by controlling the DC-link voltage and inner AC current control loop shown in Figure 2.10 [17].

2.4.3.1. DC voltage outer loop. The outer loop controls the active power flow and reactive power flow using the PI controller. The error signal generates the reference for the inner current control loop. The frequency of the outer loop is generally set low to make the outer loop less sensitive for the variation in the inner current controller. The control bandwidth of the outer loop will be in the range 10-20 Hz. Thus, it will be much slower compared to the inner loop.

2.4.3.2. AC current control loop. AC current control strategy involves feed-forward voltage control. The control scheme controls the d-axis and q-axis current from the inverter. The loop frequency will be of the order of 100 Hz, which is approximately ten times faster than the outer loop. The d-axis reference is generated from the DC voltage control, and the q-axis component is set based on the reactive power requirement of the load. After tracking the current, the d-axis and q-axis voltage component will be converted into the three-phase voltage. The next step is the gating signal generation for the inverter from the three-phase voltage. The phase-locked loop (PLL) is also required to fix the frequency of the grid.

3. UNBALANCED STUDY FOR A SINGLE PV GRID-CONNECTED SYSTEM

Due to the advancement in power electronics capability, today most of the DGs are interfaced to the utility grid via power converters. Also, the penetration of renewable energy directly into the distribution system at mid-voltage and low-voltage levels is rising owing to the improved reliability and controls available today. Because of the integration of the DGs directly with the grid, the influence study on the microgrid is essential in a steady-state as well as during an unbalance condition, which impacts the normal operating condition of a microgrid. To minimize the effects of an unbalance condition on the microgrid as well as on the connected loads, various grid codes are in place for wind generation and the PV generation system. This chapter describes various events that can cause an unbalance condition for the grid-connected PV system. Moreover, during an unbalanced event, the different grid connection requirements for the PV system are explained in detail. Next, the control algorithm design approach to meet the grid requirements is presented. Lastly, the simulation results are shown, which validate the proposed control method.

3.1. UNBALANCE TYPES CLASSIFICATION AND FAULT CATEGORIES

The major cause of an unbalance in the grid-connected system is the occurrence of the fault on the grid, because the vast majority of the loads will be connected to the grid and it is highly prone to natural disturbances or any operating errors. On the top-level classification, the faults are of two kinds: the balanced and unbalanced faults which are defined below:

Balanced fault. During this fault, all the three-phase voltage drops will be the same, which depends on the severity of the fault. The occurrence probability of this fault is extremely rare.

Unbalanced fault. During this fault, the phase-voltage drop will be uneven, which depends on the nature of the fault. The most common types of unbalanced faults are (a) Single-line-to-ground fault (SLG), (b) Line-to-line fault (LL), and (c) Line-to-line-ground fault (LLG).

From the above mentioned fault types, the SLG fault is the most common and frequently occurring fault. All these faults will register a different voltage dip, which depends on the nature and the cause of the fault. It can be further classified into different categories based on the voltage dips as presented by Giuseppe et al. in [18]. The voltage dip type depends on the fault with respect to the source under study. In this study, the voltage dip will be type A because the transformer is not considered in the system, as the study is conducted at the low-voltage level.

3.2. ADVERSE EFFECTS OF UNBALANCE ON PV SYSTEM

As explained earlier, the major reason for an unbalance in the system is a fault. The unbalance origin can be grid-side disturbances or any issue in the microgrid. However, the latter cause is rare. During an unbalance, the system performance changes significantly due to the genesis of the undesirable events that directly reduce the capability of the microgrid components. The unbalance event can cause (a) Overcurrent tripping, (b) Active and reactive power oscillations, (c) DC-link oscillation, or (d) Non-sinusoidal current injection [11].

Apart from the above mentioned issues, THD injection is also a major concern in the event of an unbalance for the grid-connected inverters. Therefore, it is of utmost importance to identify the unbalance event and restrain the fault current to the nominal current or to the magnitude that will be safe for the connected equipment of the microgrid. Moreover, various grid requirements command changes in the operation routine of the microgrid during an unbalance fault situation.

During a fault, a voltage sag occurs during which the negative sequence component will be induced in the system. This is due to the unbalance in the voltage at the PCC. This causes the generation of the negative sequence current that will flow from the microgrid to the grid if not restrained to the minimum value. Besides this, the active and reactive power will start oscillating due to the presence of the negative sequence components, which will be further explained in a later section.

Subsequently, the power oscillation induces the voltage oscillation in the DC-link with double the grid frequency, as the active power flow is controlled using the DC-link voltage loop. Therefore, the unbalance causes the cascading, which exacerbates disturbances in the PV system. Moreover, if the unbalance is sustained for a long time, then it can cause tripping of the PV system due to a very high magnitude current flow that may reach the short-circuit of the PV array. DC-link oscillations reduce the life of the capacitor link and thus it affects the overall reliability of the inverter. Therefore, fault control is desired in order to protect the microgrid components and follow the grid regulations.

3.3. LOW VOLTAGE RIDE THROUGH (LVRT)

The grid-connected microgrid follows the grid for voltage and frequency control, and shares the power according to the demand from the load. Therefore, during a fault, the inverter should disconnect if the fault is severe because it acts as the fault's current source. If all the grid-connected inverters start shutting down, then it can result in a cascading failure event of the grid that eventually leads to a total blackout of the region. To avoid this situation, the grid-connected inverters are required to follow the grid regulation. The grid regulation for the DGs is different than the synchronous generator connected to the grid because of the difference in the capability and design aspects of synchronous machines and DG. By following the grid regulation, the inverter connected to the grid will operate to
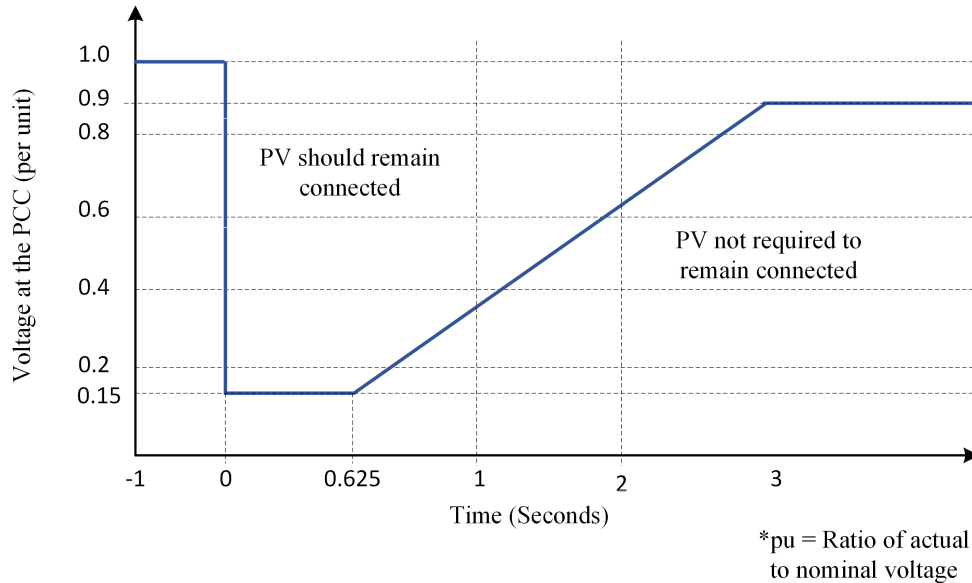
Figure 3.1. Connection requirement of PV during LVRT

support the grid based on the capability and control complexity. Hence, the grid regulation improves the overall performance of the grid-connected inverter by increasing the reliability of the grid system.

In recent years, a plethora of research works focus on the LVRT strategies of wind and PV system. As explained earlier, the faults are generally considered the major cause of the unbalance situation in the system. The unbalanced faults are the most frequent and cause a higher threat of equipment failure. Therefore, from the protection perspective, the control strategy should be designed to improve the operation strategy of the grid-connected inverter during the fault. Also, the grid regulation demands certain policies to support the grid during low voltage events. Thus, the LVRT strategy is designed to curtail the current injected by the inverter to the grid and support the grid during low voltage events [19]. Due to increasing penetration of a wind system into the grid system, earlier the LVRT is imposed for the wind system first. Nowadays, the grid regulation is imposed on the PV system too, after observing the direct grid-connection application of the PV system.
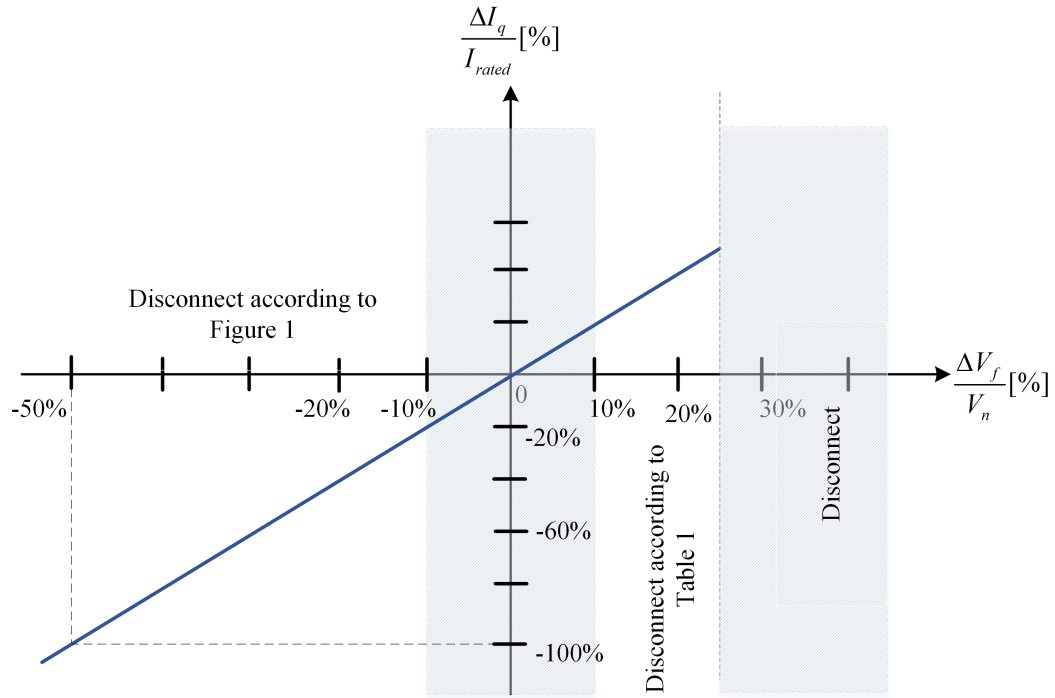
Figure 3.2. Reactive power injection criteria during LVRT

During LVRT, the grid-connected PV system should not disconnect from the utility grid immediately. In the USA, the Federal Energy Regulatory Commission (FERC) established the grid regulation for the grid-connected wind system, which is extended for the PV system and presented here. Figure 3.1 indicates the grid regulation to be followed during LVRT. The x-axis is the time passed after the fault in seconds and the y-axis indicates the voltage at the PCC in pu during a fault. According to the technical requirements, the grid-connected inverter should remain connected to the grid if the voltage at the PCC is above the curve presented in Figure 3.1. For example, if the voltage at the PCC is 0.4 pu just after the fault, then the inverter remains connected because the grid regulation criteria for tripping is 0.15 pu voltage or less during the fault. Furthermore, 0.15 pu voltage criteria at PCC is for 0.625 s, after which it ramps up until 3 s. At any time, if the voltage at the PCC is less than the voltage indicated in Figure 3.1, then the inverter can trip, or it should remain connected.

Besides the connection criteria, it is also crucial to support the grid by supplying the reactive power to help the grid in serving the connected load reactive power requirement. Though this regulation is not explicitly mentioned or imposed on the PV system, it is of higher interest considering its application in the near future. During a fault, because of the low PCC voltage, the reactive power injection is required to support the grid voltage or else it will keep falling, which eventually trips all the loads from the grid [20]. In this situation, the connected grid inverter plays a vital role in supplying higher reactive power to support the grid reactive power requirement. Moreover, the supply of reactive power should be controlled based on the severity of the fault to avoid a further complication of the excess reactive power during the fault. The illustration of the excess grid current requirement chart, based on the voltage at the PCC, is shown in Figure 3.2. It is presented in terms of the percentage of the rated current to be injected into the system. For PCC voltage of 50% and higher, the reactive current requirement varies, which can be calculated from the curve. But if the voltage at the PCC is less than 90%, the grid reactive current should be injected, which may demand approximately double the inverter nominal current during the fault.

3.4. IMPORTANCE OF INVERTER CONTROL IN LVRT

Inverters are used to interface the DGs with the grid, and now because of the continuous research and improved capability of these devices, the direct integration of the DGs with the grid is increasing. Also, the challenges involved in renewable energy integration are high but can be met with proper designing of the individual components of the integration system. Moreover, the overall performance improvement of the system depends on the operation of each block. Thus, it is required to improve the existing capabilities of the inverter. It should not just act as the power conversion unit that converts DC power to AC power and regulates the power flow, but it should also fulfill the grid regulation and limit the current as per the design. The inverter has the capability to overcome most of the operating challenges that are explained in the previous section. The overcurrent can be
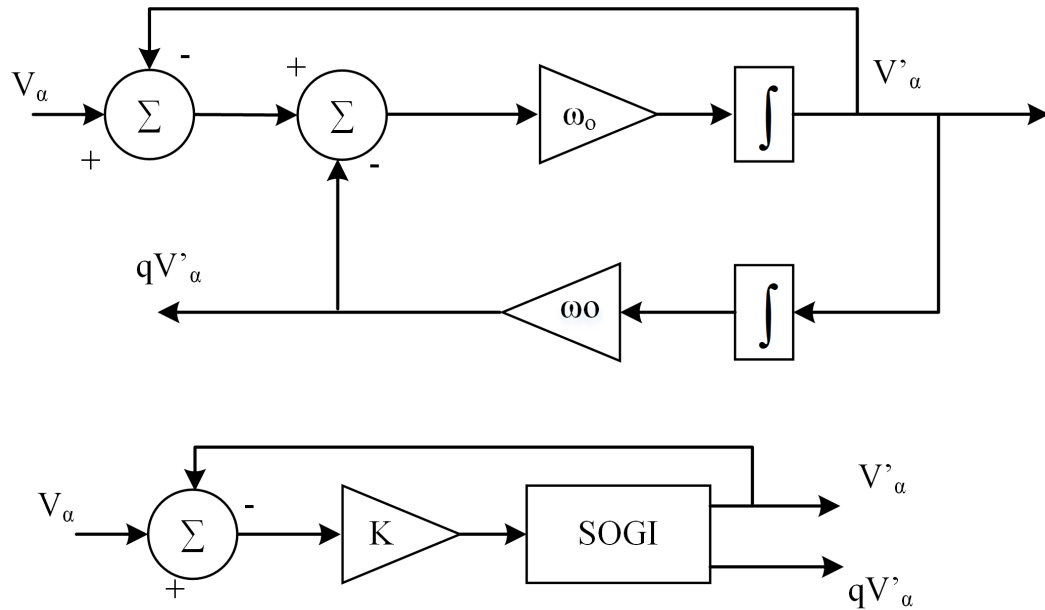
Figure 3.3. Dual second-order generalized integrator structure

limited by designing the inverter control to restrict the current to certain values based on the requirement. In addition, the active and reactive power can be controlled through the inverter control. The active power flow control will reduce the DC-link voltage oscillations which is the weaker link in the inverter system. Thus, it is clear that inverter control is a very critical factor to overcome the existing challenges for the grid-connected system.

3.5. DUAL SECOND-ORDER GENERALIZED INTEGRATOR (DSOGI)

The extraction of the positive and negative sequence is the first step of the double current control method. It can be achieved using numerous available methods. For the current work, the DSOGI method is implemented, which deploys the quadrature signal generator (QSG) along with the positive and negative sequence calculation [7].

The advantages of the DSOGI method are the accuracy, speed, and the frequency adaptiveness, which improves the overall performance of the controller. Also, it acts as the band pass filter (BPF) due to its ability to reject higher orders of the switching frequency. First, the three-phase voltage will be converted into the stationary reference frame using (2.16).

Using the SOGI-QSG method, the respective stationary voltages will be converted into the two components that are 90° apart from each other. The SOGI-QSG scheme is presented in Figure 3.3. The transfer function of the SOGI-QSG scheme is shown in (3.1) [5]:

$$
\begin{aligned}
D(s) &= \frac{v'}{v}(s) = \frac{k\omega's}{s^2 + k\omega's + \omega'^2} \\
Q(s) &= \frac{qv'}{v}(s) = \frac{k\omega'^2}{s^2 + k\omega's + \omega'^2}
\end{aligned}
\tag{3.1}
$$

here ω' is the resonant frequency, k is the damping factor, which gives the optimized performance for $k = \sqrt{2}$ in (3.1)

$$
\begin{aligned}
v' = Dv &\left\{ \begin{array}{l} |D| = \frac{k\omega\omega'}{\sqrt{(k\omega\omega')^2 + (\omega^2 - \omega'^2)^2}} \\ \arg(D) = \tan^{-1}(\frac{\omega'^2 - \omega^2}{k\omega\omega'}) \end{array} \right\} \\
qv' = Qv &\left\{ \begin{array}{l} |Q| = \frac{\omega'}{\omega}|D| \\ \arg(Q) = \arg(D) - \frac{\pi}{2} \end{array} \right\}
\end{aligned}
\tag{3.2}
$$

The qv' will always lag v' by 90° as presented in (3.2). These signals will be converted into the positive and negative sequence $\alpha\beta$ voltages using an arithmetic operation, also called the sequence calculator as presented in (3.3)

$$
\begin{aligned}
V_\alpha{}^+ &= \frac{v_\alpha' + qv_\beta'}{2} \\
V_\beta{}^+ &= \frac{v_\beta' - qv_\alpha'}{2} \\
V_\alpha{}^- &= \frac{v_\alpha' - qv_\beta'}{2} \\
V_\beta{}^- &= \frac{qv_\alpha' + v_\beta'}{2}
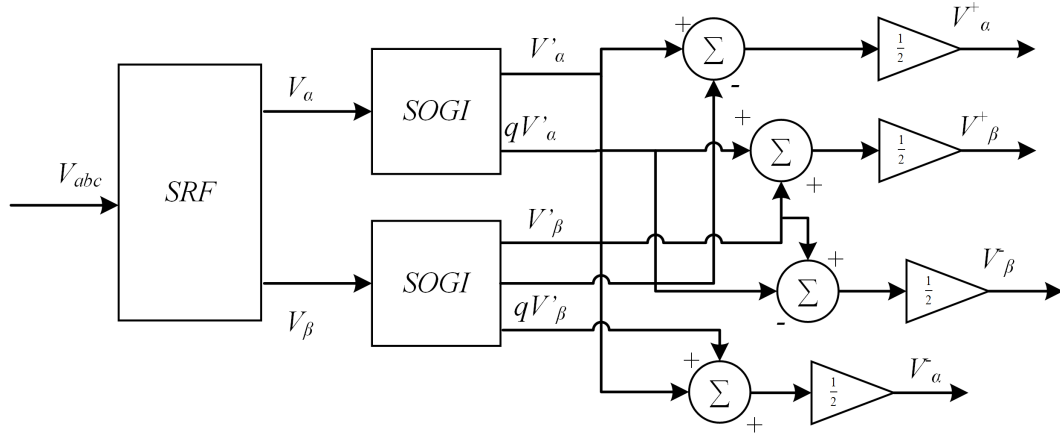\end{aligned}
\tag{3.3}
$$

Figure 3.4. Positive and negative sequence calculation

The same method is valid to extract the positive and negative sequence components of the current as presented in Figure 3.4. Furthermore, the stationary voltage/current is converted into the rotating reference frame of d-axis and q-axis components using the transformation in (2.17). The value of θ will be positive or negative, which can be calculated using (3.4).

$$
|V^+|'= \sqrt{(V_\alpha{}^+)^2 + (V_\beta{}^+)^2}
$$
$$
\theta^+ = \tan^{-1}\frac{v_\beta{}^+}{v_\alpha{}^+}
$$

(3.4)

The separation calculation of θ^+ and θ^- is required for the separate positive and negative d-axis and q-axis component calculations.

3.6. DETAIL INVERTER CONTROL DESIGN FOR THE CURRENT WORK

This section describes the detail inverter control design process used in the current work. The complete implementation of the design process is presented in Figure 3.5. The control algorithm has two inputs, namely inverter current flowing through the filter
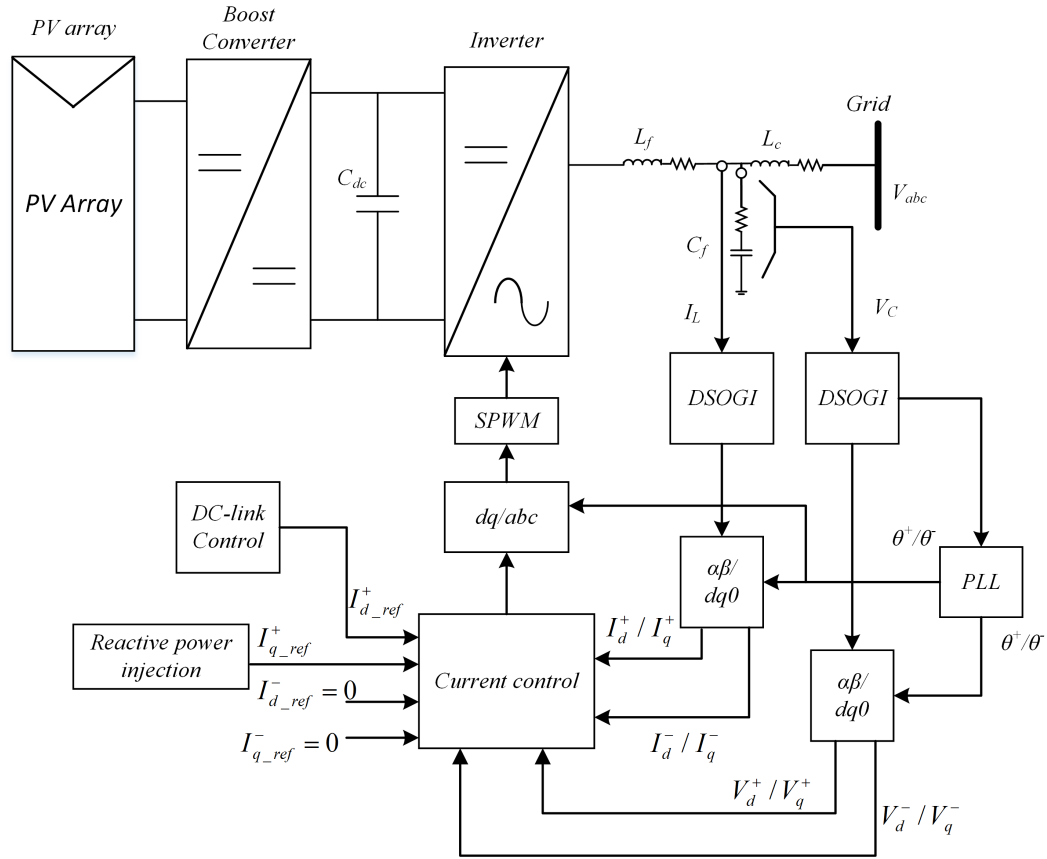
Figure 3.5. Inverter controller complete block diagram

inductor and the voltage measured across the capacitor. The inverter control design process is divided into the following subsections for the step-by-step analysis and the deep insight of the control process.

3.6.1. Sequence Extraction using DSOGI Method. The first step of the inverter design is the extraction of the positive and negative sequence using the DSOGI method. The input to the DSOGI-BPF is V_α, which is calculated using *abc* to $\alpha\beta$ transformation using (2.16). The sequence calculation block shows the arithmetic operation of the output of the DSOGI-BPF filter, which is presented in Figure 3.5. The value of ω' and k used in

this work is 377 rad/s and 1.2, respectively. The phase-locking is to be separated for the positive and negative sequence because of the opposite rotation of the positive and negative sequence. The separate phase-locking is implemented using (3.4).

3.6.2. Reference Frame Transformation. The next step is the conversion of the stationary reference frame $\alpha\beta$ to the rotating reference frame dq using (2.17). The angle θ^+ and θ^+ are calculated from the positive and negative sequence stationary voltages, respectively using (3.4). The phase-locking angles θ^+ and θ^+ are used for the current transformation process, too.

3.6.3. Current Reference Generation. The purpose of the CRG is the appropriate selection of the current references for the control purpose of the positive and negative d-axis and q-axis currents. Moreover, the setting of the CRG value depends on the operation requirements of the inverter. The CRG generation here focuses on the unity power factor operation, constant average active power injection, reactive power injection, and the symmetrical current injection into the grid. In addition, the CRG selection approach accounts the DC-link voltage oscillations reduction during the fault. Because of the separation of the positive and negative sequence control, the voltage in the rotating reference frame can be represented as in (3.5):

$$V_{dq} = V_{dq}^{p} e^{j\omega t} + V_{dq}^{n} e^{-j\omega t} \tag{3.5}$$

here V_{dq}^{p} and V_{dq}^{n} are positive and negative dq voltages, respectively. Also, the current can be represented as in (3.6)

$$I_{dq} = I_{dq}^{p} e^{j\omega t} + I_{dq}^{n} e^{-j\omega t} \tag{3.6}$$

Thus, the total apparent power can be calculated using (3.7)

$$S = (V_{dq}^{p} e^{j\omega t} + V_{dq}^{n} e^{-j\omega t})(I_{dq}^{p} e^{j\omega t} + I_{dq}^{n} e^{-j\omega t})^{*} \tag{3.7}$$

Equation (3.7) can be further simplified as $S = P + jQ$, where P and Q are the instantaneous active and reactive power flowing through the inverter [8]. The instantaneous real and reactive power can be further broken down into the combination of average and oscillating components as

$$P(t) = P_o + P_1 cos(2\omega t) + P_2 sin(2\omega t)$$
$$Q(t) = Q_o + Q_1 cos(2\omega t) + Q_2 sin(2\omega t)$$

(3.8)

here P_o and Q_o are the average active and reactive power, whereas P_1, P_2, Q_1, and Q_2 are the higher-order oscillating components of the active and reactive power:

$$P_o = 1.5(V_d^+ I_d^+ + V_q^+ I_q^+ + V_d^- I_d^- + V_q^- I_q^-)$$
$$P_1 = 1.5(V_d^+ I_d^- + V_q^+ I_q^- + V_d^- I_d^+ + V_q^- I_q^+)$$
$$P_2 = 1.5(V_q^- I_d^+ - V_d^- I_q^+ - V_q^+ I_d^- + V_d^+ I_q^-)$$
$$Q_o = 1.5(V_q^+ I_d^+ - V_d^+ I_q^+ + V_q^- I_d^- - V_d^- I_q^-)$$
$$Q_1 = 1.5(V_q^+ I_d^- - V_d^+ I_q^- + V_q^- I_d^+ - V_d^- I_q^+)$$
$$Q_2 = 1.5(V_d^+ I_d^- + V_q^+ I_q^- - V_d^- I_d^+ - V_q^- I_q^+)$$

(3.9)

During normal operating conditions, the oscillating components P_1 and P_2 will be zero because of the absence of negative sequence components in the voltage and current. Thus, the active power flow will be constant. As soon as the fault initiates, due to the presence of the negative sequence components, P_1 and P_2 will be non-zero, which is to be nullified to keep the active power flow constant during the fault. To set the CRG in terms of the power components, the matrix conversion is performed as presented in (3.10):

$$\begin{pmatrix} \frac{2}{3}P_o \\ \frac{2}{3}Q_o \\ \frac{2}{3}P_1 \\ \frac{2}{3}P_2 \end{pmatrix} = \begin{pmatrix} V_d^+ & V_q^+ & V_d^- & V_q^- \\ V_q^+ & -V_d^+ & V_q^- & -V_d^- \\ V_q^- & -V_d^- & -V_q^+ & V_d^+ \\ V_d^- & V_q^- & V_d^+ & V_q^+ \end{pmatrix} \begin{pmatrix} I_d^+(t) \\ I_q^+(t) \\ I_d^-(t) \\ I_q^-(t) \end{pmatrix}$$

(3.10)

It can be further solved by expressing the current matrix in terms of the power matrix as shown in (3.11)

$$
\begin{pmatrix} I_d^+(t) \\ I_q^+(t) \\ I_d^-(t) \\ I_q^-(t) \end{pmatrix} = \begin{pmatrix} V_d^+ & V_q^+ & V_d^- & V_q^- \\ V_q^+ & -V_d^+ & V_q^- & -V_d^- \\ V_q^- & -V_d^- & -V_q^+ & V_d^+ \\ V_d^- & V_q^- & V_d^+ & V_q^+ \end{pmatrix}^{-1} \begin{pmatrix} \frac{2}{3}P_o \\ 0 \\ 0 \\ 0 \end{pmatrix}
\tag{3.11}
$$

The above matrix can be further simplified as shown in (3.12)

$$
\begin{pmatrix} I_d^+(t) \\ I_q^+(t) \\ I_d^-(t) \\ I_q^-(t) \end{pmatrix} = \frac{2P_o}{3M} \begin{pmatrix} V_d^+ \\ V_q^+ \\ -V_d^- \\ -V_q^- \end{pmatrix}
\tag{3.12}
$$

here $M = [(V_d^+)^2 + (V_q^+)^2] - [(V_d^-)^2 + (V_q^-)^2]$ is a variable that depends on positive and negative d-axis and q-axis voltage. Thus, for the zero active power oscillations and unity power factor operations, the CRG values are shown in (3.13):

$$
\begin{pmatrix} I_d^+(t) \\ I_q^+(t) \\ I_d^-(t) \\ I_q^-(t) \end{pmatrix} = \frac{2P_o}{3M} \begin{pmatrix} V_d^+ \\ 0 \\ 0 \\ 0 \end{pmatrix}
\tag{3.13}
$$

The above expression of D can be further simplified to V_d^+ since V_q^+ is tracked to zero. Also, V_d^- and V_q^- have very small magnitude and are thus neglected for the CRG calculation. Thus, the final expression for the constant average power injection into the grid is calculated

using (3.14)

$$
\begin{pmatrix} I_d^+(t) \\ I_q^+(t) \\ I_d^-(t) \\ I_q^-(t) \end{pmatrix} = \frac{2P_o}{3(V_d^+)^2} \begin{pmatrix} V_d^+ \\ 0 \\ 0 \\ 0 \end{pmatrix}
\tag{3.14}
$$

The above selection of CRG fulfills the criteria of the zero average power oscillations, due to consideration of oscillating components to zero. Furthermore, the unity power factor is also achieved because of the zero average reactive power injection. The note should be taken that the total reactive power will oscillate because of the presence of the negative sequence components, although the average reactive power injection would be zero. The complete elimination of the active and reactive power oscillation cannot be achieved simultaneously because of the limited degree of freedom of the matrix calculation. Therefore, either active or reactive power can be eliminated at a time. The reference value presented in (3.14) is selected for the current tracking purpose for the PI control.

The power calculation is very complex in dq reference frame as presented in (3.9); thus, the power calculation is performed in $\alpha\beta$ reference frame using equation (3.15) [11]

$$
\begin{aligned}
P &= P_o + P_{osc} \\
P_o &= 1.5(v_\alpha^+ i_\alpha^+ + v_\beta^+ i_\beta^+ + v_\alpha^- i_\alpha^- + v_\beta^- i_\beta^-) \\
P_{osc} &= 1.5(v_\alpha^+ i_\alpha^- + v_\beta^+ i_\beta^- + v_\alpha^- i_\alpha^+ + v_\beta^- i_\beta^+) \\
Q &= Q_o + Q_{osc} \\
Q_o &= 1.5(v_\beta^+ i_\alpha^+ - v_\alpha^+ i_\beta^+ + v_\beta^- i_\alpha^- - v_\alpha^- i_\beta^-) \\
Q_{osc} &= 1.5(v_\beta^+ i_\alpha^- - v_\alpha^+ i_\beta^- + v_\beta^- i_\alpha^+ - v_\alpha^- i_\beta^+)
\end{aligned}
\tag{3.15}
$$

To fulfill the reactive power injection requirement, the CRG value should be chosen based on the voltage level at PCC during the voltage sag event from the chart presented in Figure 3.2. According to Figure 3.2, for the voltage rise at the PCC that will fall in the right half of the plane, the inverter should not supply any reactive power and should disconnect

based on the voltage criteria mentioned in Table 3.1 [20]. For the pu voltage sag at the PCC less than 0.9, 2% of reactive current should be injected for 1% voltage drop at the PCC. The injection of the reactive power along with the active power increases the burden on the PV system. Also, the power capability of the PV system should not increase its rated capacity. To restrict the total power flow from the grid, the active power flow and the reactive power flow balance should be achieved. Moreover, the current should not exceed the current capability of the inverter, which is generally taken as twice the rated current of the inverter. Thus, I_d^+ and I_q^+ should be controlled to inject the active and reactive power into the system and also limit the current through the inverter [21]. Therefore, first I_q^+ should be calculated to be injected into the system and then I_d^+ should be set, which does not exceed the current capacity of the inverter as shown in (3.16)

$$I_d^+ = \sqrt{(2I_{rated})^2 - I_q^{+2}}$$ (3.16)

The reference is calculated using Equation (3.17) which satisfies the reactive current injection criteria in Figure 3.2

$$
\begin{aligned}
I_q^+ &= 0 & \frac{V_1}{V_N} &> 0.9 \\
I_q^+ &= (2 - 2\frac{V_1}{V_N})I_{rated} & \frac{V_1}{V_N} &\leq 0.9
\end{aligned}
$$ (3.17)

Table 3.1. LVRT disconnection requirement based on voltage magnitude

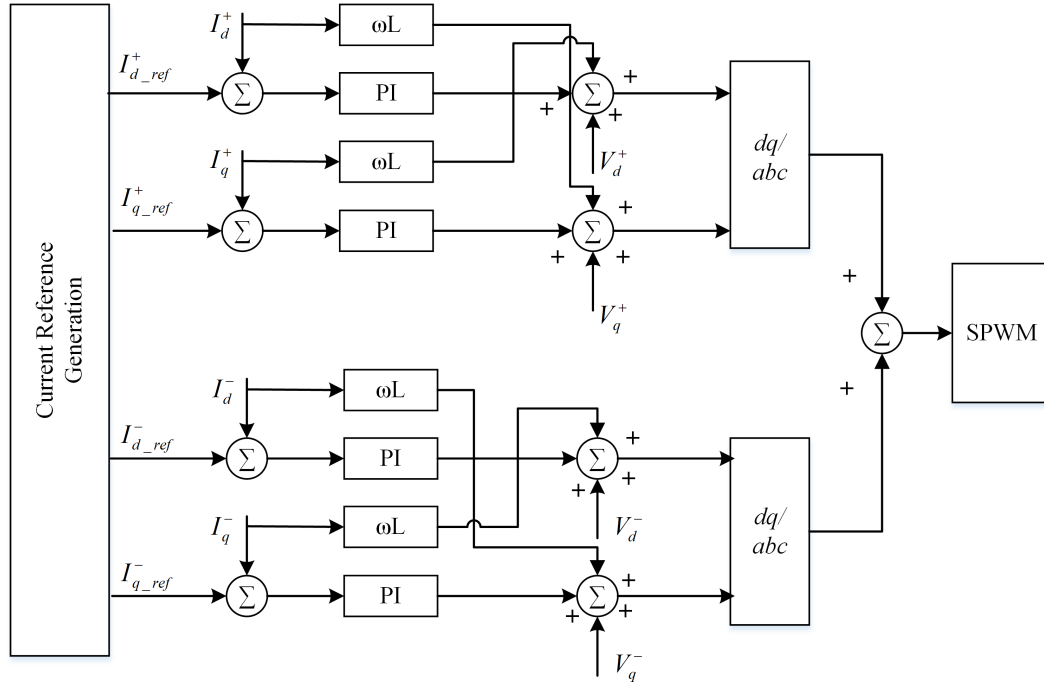| Voltage V (%)	Minimum trip time (cycles) (60 Hz)
$100 \leq V < 110$	Not fixed
$110 \leq V < 120$	60
$120 \leq V < 125$	10
$125 \leq V$	Instantaneous

Figure 3.6. Inverter dual current control

According to (3.17), during voltage sag, if the pu voltage at the PCC is greater than 0.9, then no reactive current will be injected into the system. If the voltage at the PCC is less than or equal to 0.9, then the reactive current will be commanded based on the voltage dip at the PCC. This will ensure the appropriate level of the reactive current injection, which eventually injects the reactive power into the grid. In addition, the CRG calculation method guarantee the current limiting to the safest value for the inverter.

3.6.4. PI Control. A classical PI control approach is used for the inverter control purpose that involves the use of the proportional gain and integrator for controlling the specific state of the physical system. The outer loop of the proposed controller is the DC-link voltage control or active power flow control. The error signal is multiplied with the reference DC voltage to obtain the average active power reference.

Using the CRG values as per (3.14), the positive and negative sequence currents are tracked as shown in Figure 3.6. The feed-forward voltage is added to the respective voltage calculation as presented in (2.13). Finally, the d-axis and q-axis commanded voltages are generated using (2.13). The commanded voltages u_d and u_q are present in the rotating reference frame, which needs to be converted into *abc* voltages using the back-reference frame transformation conversion process. The conversion from dq components to $\alpha\beta$ can be achieved using (3.18).

$$\begin{pmatrix} V_\alpha \\ V_\beta \end{pmatrix} = \begin{pmatrix} \sin\theta & \cos\theta \\ \cos\theta & -\sin\theta \end{pmatrix} \begin{pmatrix} V_d \\ V_q \end{pmatrix} \tag{3.18}$$

After obtaining the stationary reference frame components, the three-phase components are calculated using (3.19).

$$\begin{aligned} V_a &= V_\alpha \\ V_b &= \frac{-V_\alpha}{2} - \frac{\sqrt{3}}{2}V_\beta \\ V_c &= \frac{\sqrt{3}}{2}V_\beta - \frac{V_\alpha}{2} \end{aligned} \tag{3.19}$$

Furthermore, the gating signal for each three-pole of the inverter is obtained using (3.20).

$$m_{a,b,c} = \frac{2V_{a,b,c}}{V_{dc}} \tag{3.20}$$

The modulating signal drives the SPWM of the inverter to obtain the desired voltage at the respective pole of the inverter.

3.6.5. Boost Controller and Inverter Controller Tuning. The tuning of the boost controller and the inverter controller is achieved manually. The reason for the application of manual tuning is the complexity involved in the circuit. There are number of tuning methods available that implement the small signal analysis studies for the boost and the inverter controller. Most of these studies focus on the tuning of the partial circuit like either control of the boost converter or inverter. Here, the boost control system involves the

double loop control, as discussed previously. Thus, manual tuning is performed to obtain the optimized performance of the system, which attains the balanced condition faster. First, the inner loop is tuned using initialization of K_p and K_i values to 1 and 10. Generally, the integrator gain would be set approximately 10 times the proportional gain value, and it is a good initialization point to manually tune the circuit. The selection of K_p and K_i values depend on the design requirements of the system. K_p increases the rise time of the system, while K_i reduces the steady-state error of the control parameter. The optimization of both K_p and K_i will achieve the desired response in terms of the rise time, overshoot, and steady-state error. The design requirement here is the fast response up to 0.4 s and negligible steady-state error for controlled parameters either in the boost converter or inverter. Having achieved the inner loop tuning, the outer loop tuning is achieved using the same procedure. The gain values for the boost dual loop controller and inverter controller is presented in Table 3.2 and Table 3.3, respectively. The advantage of the manual tuning here is the consideration of the entire system, and observation of the effects of tuning on the boost converter and inverter performance.

Table 3.2. Boost controller gain

	Gain Parameters	Values
Outer voltage loop	K_p	0.1
	K_i	2
Inner current loop	K_p	0.6
	K_i	6

Table 3.3. Inverter controller gain

	Gain Parameters	Values
Outer voltage loop	K_p	1
	K_i	10
Inner current loop	K_p	5
	K_i	50

3.7. SIMULATION RESULTS

The complete switching model is built in the MATLAB/PLECS environment. The physical components include a PV array, a boost converter, an inverter, an LCL filter, and the utility grid are modeled in PLECS. The control algorithm of the inverter is designed in the MATLAB environment. The physical system parameters used in this work are presented in Table 3.4. For the PV array, the sun insolation level and the temperature are assumed constant

Table 3.4. System physical parameters

Parameters	Values
Boost switching frequency	50 kHz
Inverter switching frequency	20 kHz
Grid RMS voltage (LL)	207 V
Inverter side filter	4.2 mH
Inverter side filter resistance	0.5 Ω
Capacitance of the LCL filter	15 μF
Capacitance damping resistance	2 Ω
Grid side coupling filter	0.5 mH
Coupling filter resistance	0.6 Ω
Nominal power	10.4 kW
dc-link capacitor	50 mF

during this study. The sun insolation level and temperatures considered are 1 kW/m^2 and 25° C. The output voltage and the current from the PV array are presented in Figure 3.7 and Figure 3.8. The steady-state voltage and current from the PV array are approximately 704 V and 14.76 A, which are nothing but the voltage and current corresponding to the maximum power output from the PV array. These results also verify the performance of the MPPT algorithm to track the maximum power from the PV array. The output current from the boost converter is presented in Figure 3.9, which presents the DCM operation of the boost converter. The normal operating condition of the complete system is simulated first to observe the stability and performance of the system. The injected voltage and current from
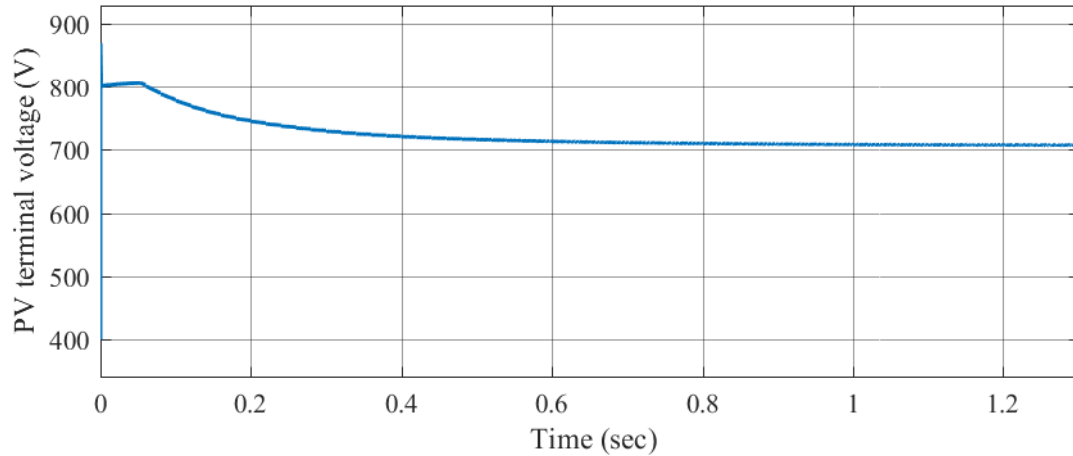
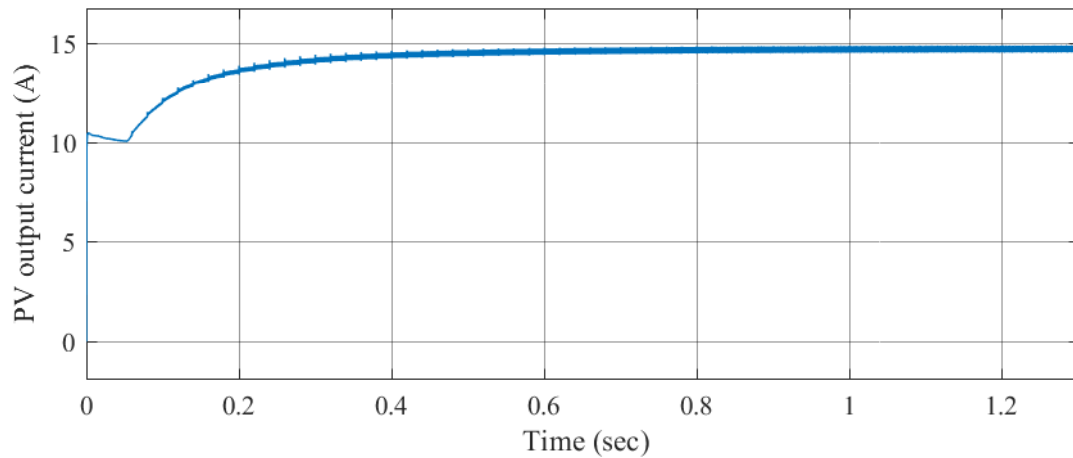Figure 3.7. PV terminal voltage having SLG fault after t = 0.8 s

Figure 3.8. PV output current having SLG fault after t = 0.8 s

the inverter are presented in Figure 3.10. The measured peak voltage is the capacitor voltage of the LCL filter. The peak value of the injected current into the grid is approximately 33.5 A. Both current and voltage are balanced and attain a steady-state at t = 0.15 s.

The symmetrical nature and less distortion in the injected current indicate the efficacy of the dual current control method. The starting transients eventually settle at 0.1 s. The output power of the PV is 10400 W. The DC-link voltage is presented in Figure 3.11,
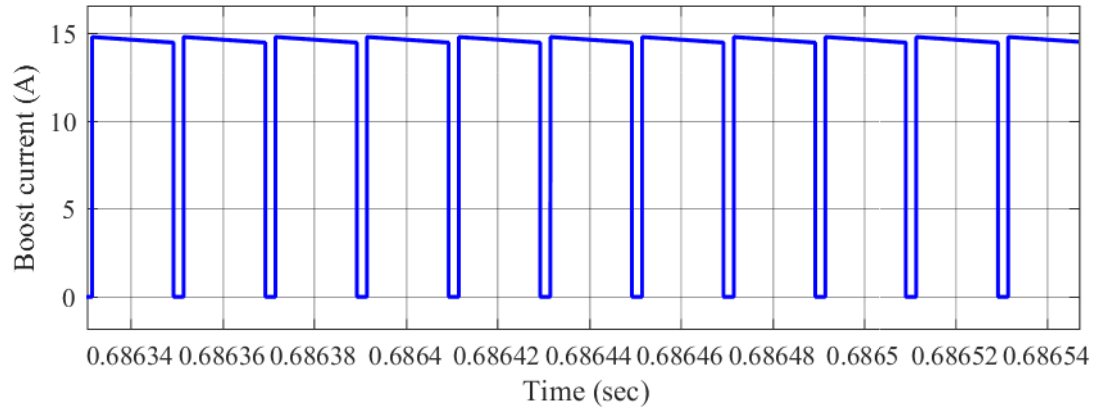
Figure 3.9. Boost output current during normal condition (zoom-in version)
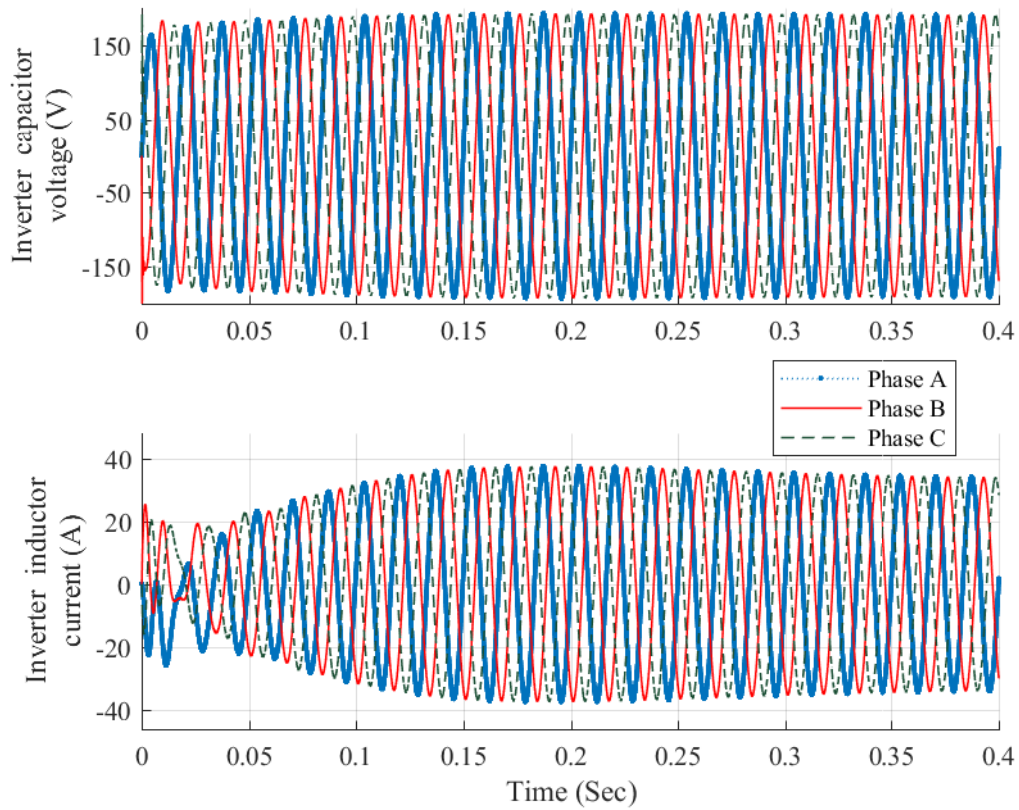

Figure 3.10. Inverter inductor current and capacitor voltage during normal condition
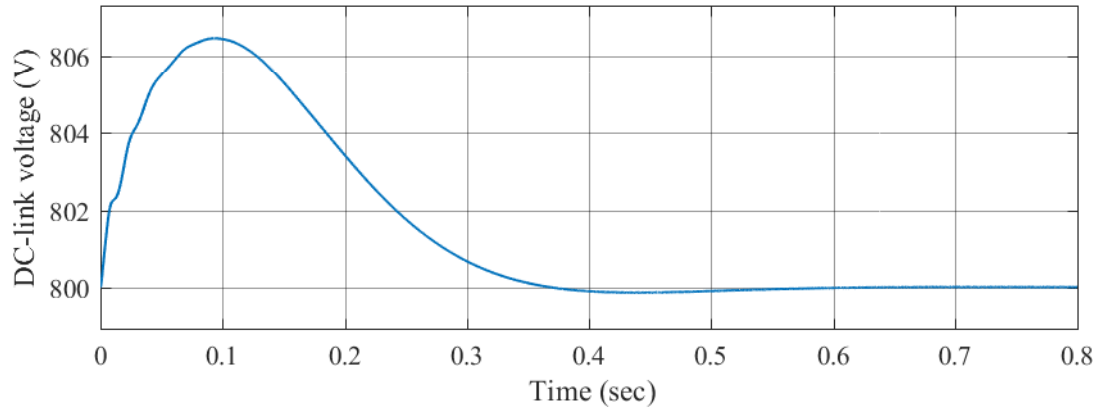
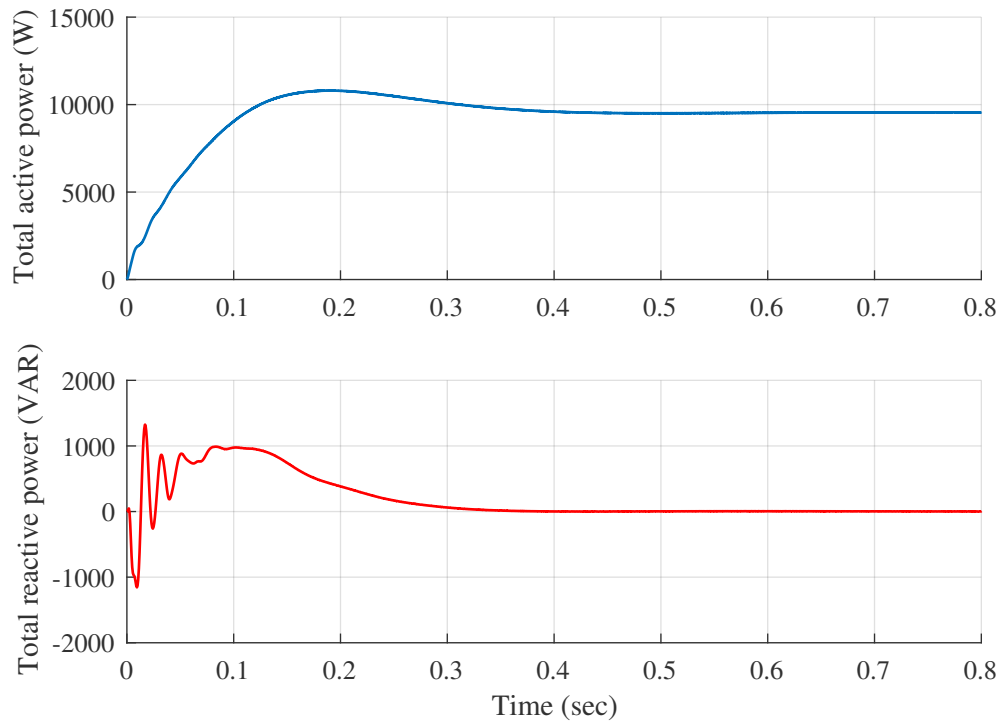Figure 3.11. DC-link voltage during normal operating condition

Figure 3.12. Total active and reactive power injection during normal operating condition

which overshoots to 6.2 V during starting and attends a steady-state at t= 0.5 s. The total active and reactive power injected into the grid is shown in Figure 3.12. The reactive power injection is zero, due to the unity power factor (UPF) condition.

To validate the efficacy of the proposed controller, the SLG fault is simulated at PCC as shown in Figure 3.13. To obtain the effect of the SLG fault, the phase voltage of a-phase at the PCC is reduced to 0.5 pu at t = 0.8 s. The reference current values are selected as
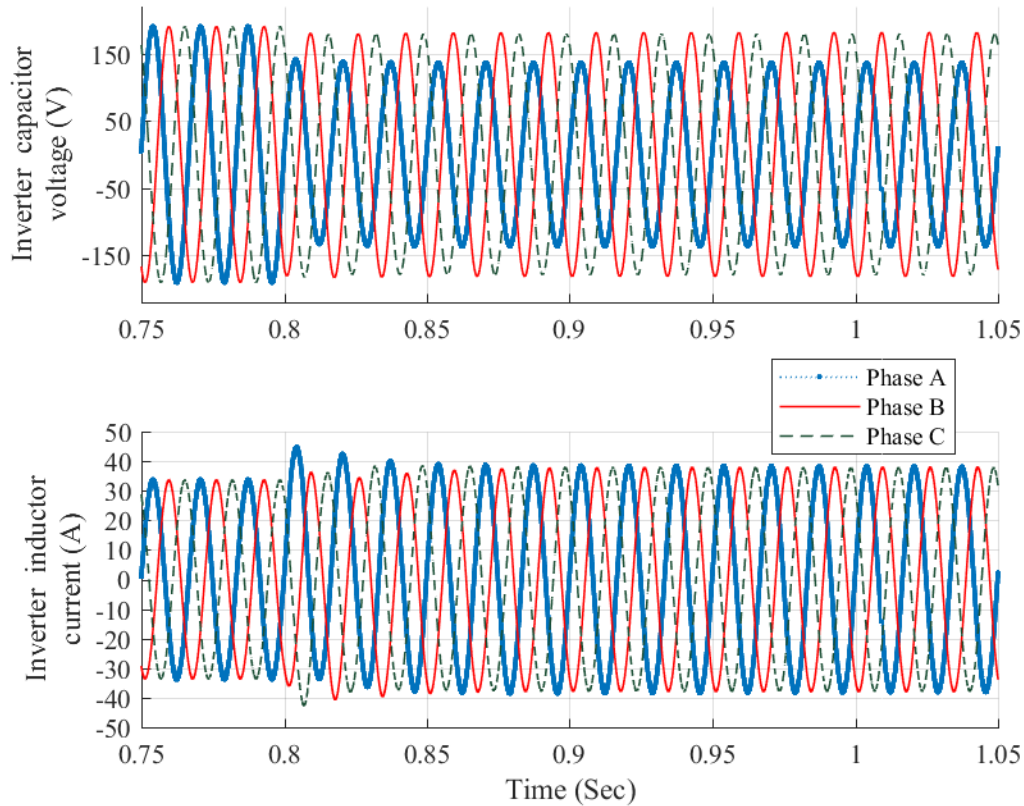

Figure 3.13. Inverter capacitor voltage and inductor current during LVRT for UPF

per (3.14). The reference value of the negative sequence d-axis and q-axis is considered zero to suppress the negative sequence component flow through the inverter. Figure 3.13 represents the voltage and current of the inverter. At t = 0.8 s, the fault initiates, which can be observed by the voltage drop of the grid. The current shoots initially due to the sudden transient that decays fast at t = 1.0 s.

The d-axis and q-axis voltages can be seen in Figure 3.14. The control design focuses on the reduction of the DC-link oscillations via the active power control. Figure 3.13 shows the three-phase current injected during the fault, which is nearly balanced. This is achieved
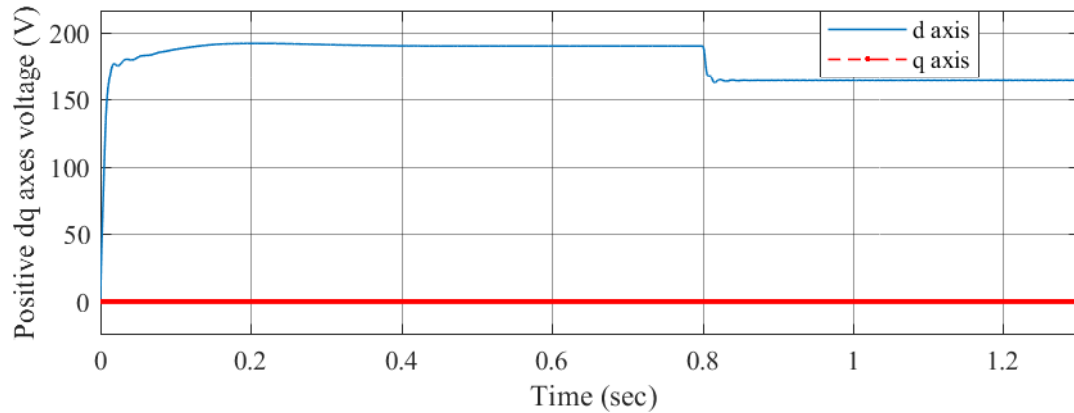
Figure 3.14. Positive sequence dq voltage across capacitor during normal condition as well as during LVRT for UPF after t = 0.8 s
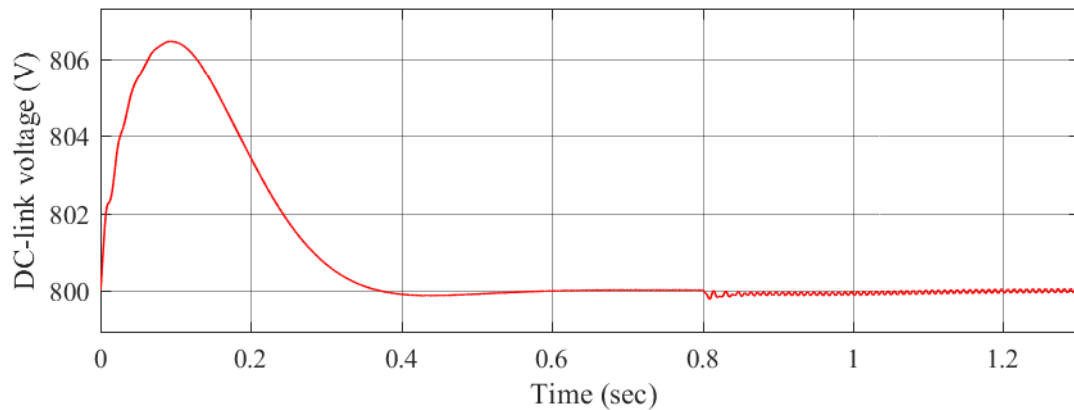

Figure 3.15. DC-link capacitor oscillations during normal condition as well as LVRT for UPF after t = 0.8 s

by controlling the negative d-axis and q-axis currents to zero. In addition, the UPF operation is also achieved by setting the reference q-axis of the positive component to zero, which ensures the zero reactive power injection into the system.

Moreover, the DC-link voltage oscillations are also eliminated as presented in Figure 3.15. The total active and reactive power injected into the grid can be observed in Figure 3.16, respectively. The above results validate the efficacy of the proposed CRG
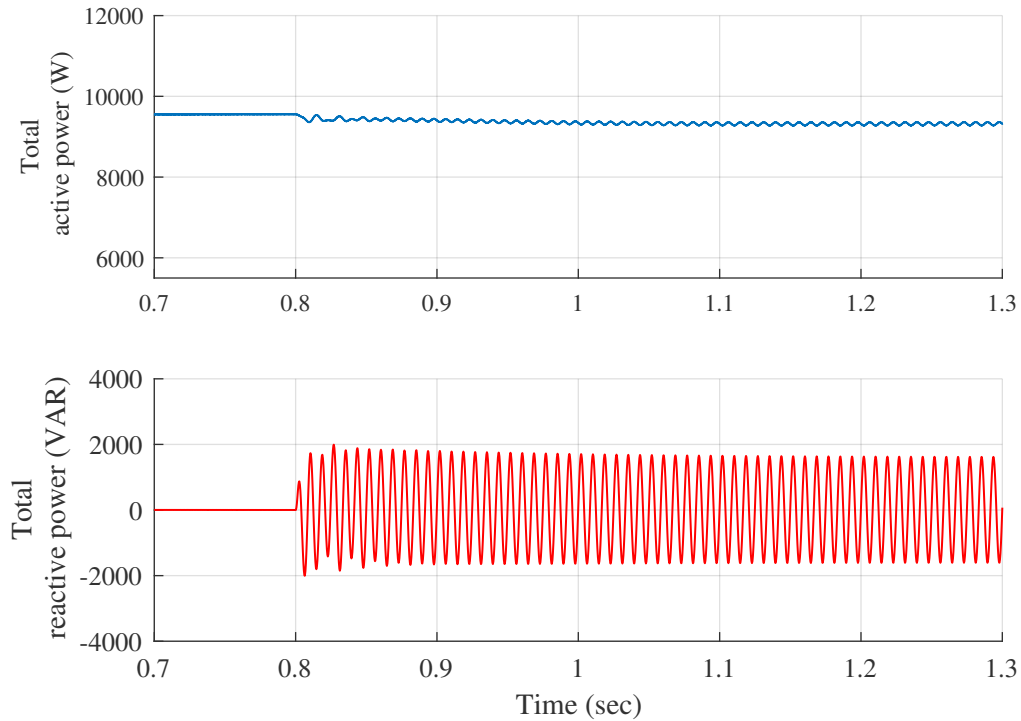
Figure 3.16. Total active and reactive power oscillations during LVRT for UPF condition

method for the active power flow control to reduce the DC-link voltage oscillations during the fault.

In order to validate the reactive power injection criteria during a fault, the SLG fault is run at the PCC having a voltage dip of 0.5 pu, similar to the previous case. The CRG is set based on Equation 3.18, which will add I_q^+ into the system based on the voltage dip. Figure 3.17 represents the average active and reactive power injection into the system, which is almost constant with a ripple of very small magnitude of double frequency component. The total active and reactive power oscillate with double the grid frequency, as can be seen in Figure 3.18. The positive and negative sequence currents are plotted in Figure 3.19.
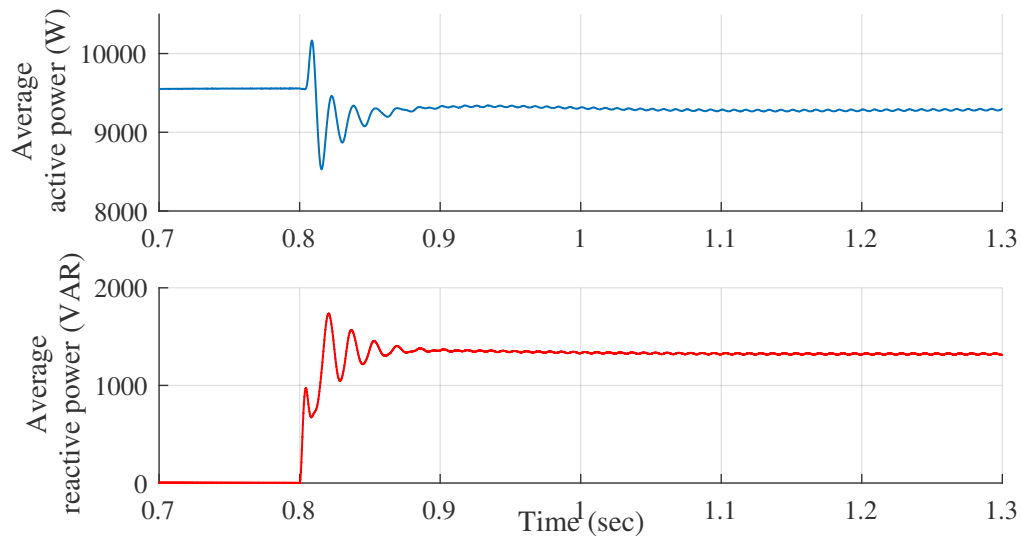
Figure 3.17. Average active and reactive power during reactive power injection condition
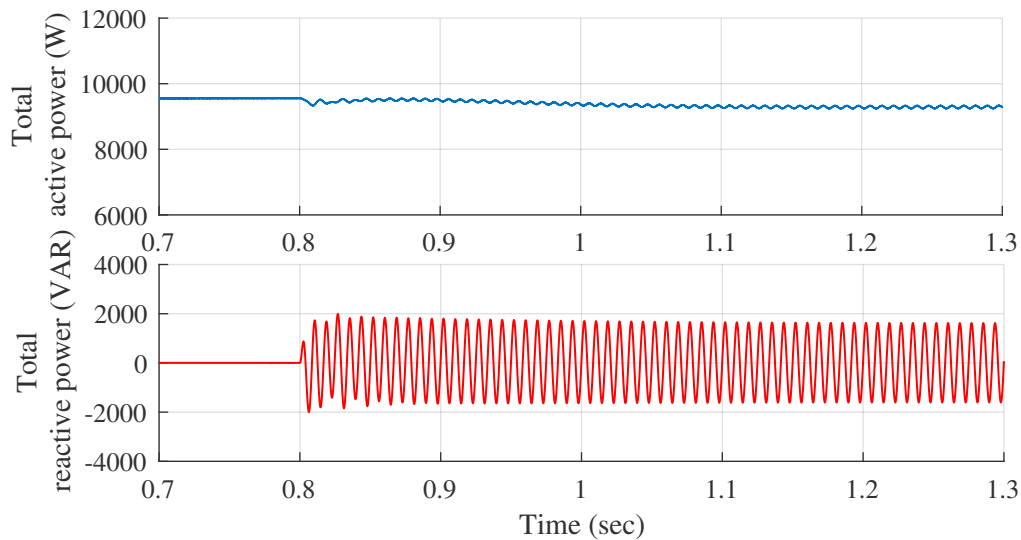

Figure 3.18. Total active and reactive power oscillations during reactive power injection condition

During LVRT, the positive d-axis and q-axis currents are injected as per the control design, and negative sequence currents are controlled to zero. The injected current into the grid is presented in Figure 3.20. The current profile is balanced owing to the fact that the negative sequence currents are controlled to zero. Thus, the reactive power injection criteria is met to support the grid during the fault.
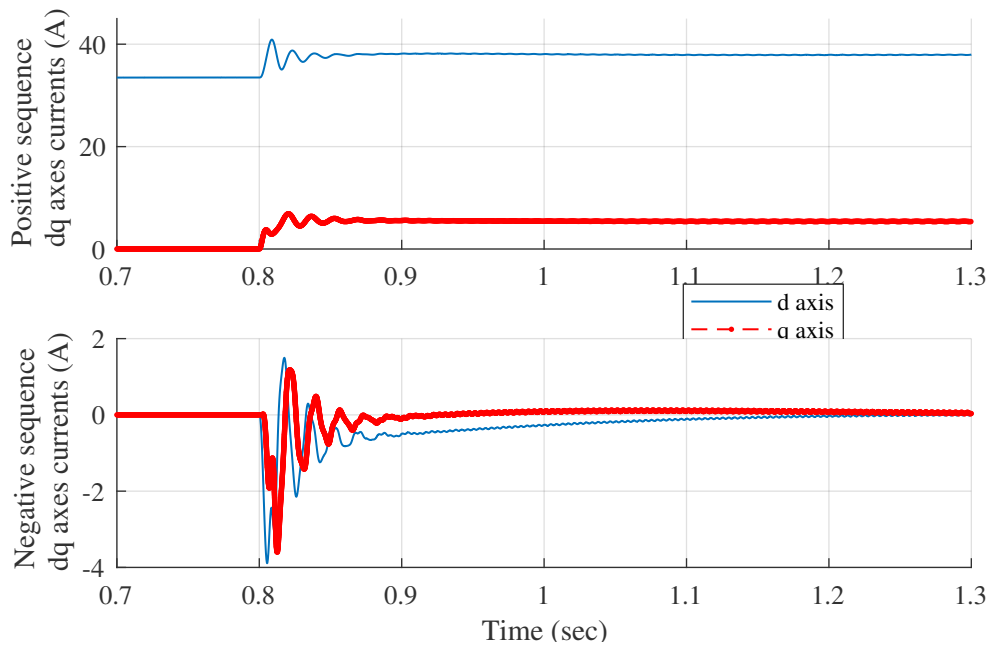
Figure 3.19. Positive and negative dq axes currents during reactive power injection condition
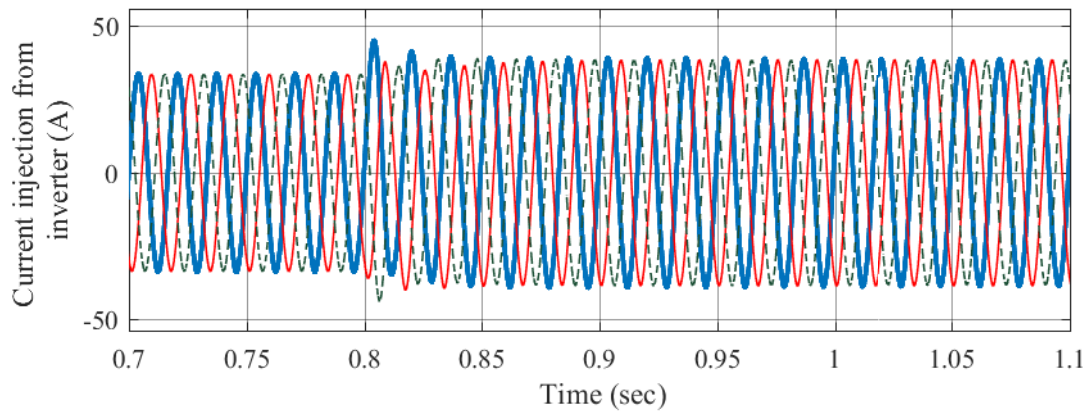

Figure 3.20. Three-phase injected current during reactive power injection condition

In summary, Figures 3.8 and 3.9 present the PV terminal voltage and output current, which indicates stable operation even during a fault after t = 0.8 s. Figures 3.11, 3.12, and 3.13 show the parameters during stable operating condition of the system. Figures 3.14 and

3.15 indicate the *dq* axis voltage of the capacitor and DC-link during normal and LVRT mode for UPF condition starting after t = 0.8 s. Figures 3.17 to 3.20 represent various parameters of the system after the LVRT at t = 0.8 s for the reactive power injection mode.

Thus, the proposed controller design can operate in UPF mode or active power injection mode, as presented in these figures. It validates the grid regulation compliance in connection and reactive power injection requirement during LVRT.

4. GRID-CONNECTED PV AVERAGE NONLINEAR MODELING

Simulating a switching model that consists of a multiple PV grid-connected system in any software environment is challenging because of the computational intensity and number of switching components present in the system. To overcome this challenge, the average nonlinear equivalent model of the single PV system is designed. The major contribution towards the slow speed of the switching model is the switching components involved in the model. Thus, to increase the speed of the model, the boost converter and the inverter are replaced by the average equivalent nonlinear model. This modification eliminated the switching from the model and eventually increased the speed of the simulation. The results are validated with the switching model to assess the accuracy of the design. To design the entire two-stage grid-connected PV model, first the boost converter nonlinear average model is designed, and then the inverter modeling is performed. After completing the separate modeling, finally, both models are integrated to form the complete grid-connected PV system. This model serves as the primary building block for the multiple PV grid-connected system. The stability study is carried out for the validation of the proposed design into the simulation environment.

The average model is commonly used to study the steady state and dynamic response of the converter and the inverter. The average models are nonlinear and time-invariant thus, the results obtained can be used for design and analysis of a grid-connected PV system. Also, the nonlinear average model can be used to obtain the small-signal model over the constant operating condition for the circuit. It averages the signal, and thus simulation can take a large step to solve and reduce the total time of simulation. Therefore, the large signal average models are used for the parallel converter study, which otherwise would be a time-consuming process due to the switching involved.
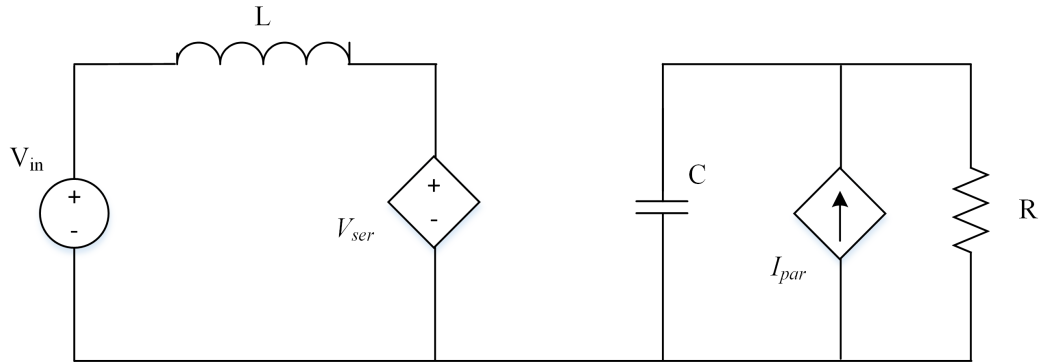
Figure 4.1. Average model of a boost converter

4.1. BOOST CONVERTER AVERAGE MODELING

To model the large-signal model of the boost converter, the switching components are replaced by the equivalent controlled voltage or current sources, as presented in Figure 4.1. The physical components are the same as the switching model, which are presented in Table 3.4. The inductor series voltage is calculated using (4.1).

$$V_{ser} = V_o(1 - D) \tag{4.1}$$

here V_{ser} is the controlled voltage source, which depends on V_o and D of the circuit. The parallel current controlled source is calculated using (4.2).

$$I_{par} = I_L(1 - D) \tag{4.2}$$

here I_{par} is the current source, which depends on I_L and duty ratio D. The model designed here operates in continuous conduction mode (CCM). Also, the capacitor value is kept large enough to maintain the constant DC-link voltage. The common practice involves the use of the load resistance at the output of the boost converter, but here the output is the parallel current controlled source that compensates the current flowing through the inverter

as presented in Figure 4.2. During the initial development stage, the modeling design is validated by connecting the load resistance of 100 Ω. The control design is the same as the switching model that injects the constant current into the DC-link. The outer loop is the voltage controlled loop for maintaining the PV terminal voltage, and the inner loop maintains the current from the PV array. The error signal will generate the duty ratio for the boost converter. The voltage reference is set constant at 704 V corresponding to the voltage at the maximum power, which replaces the function of MPPT for the model.

4.2. INVERTER AVERAGE MODELING

The large-signal average model of the inverter contains the controlled voltage source for the replacement of the inverter switches, as presented in Figure 4.2. The controlled voltage source is the three-phase voltage that drives the inverter circuit. The remaining
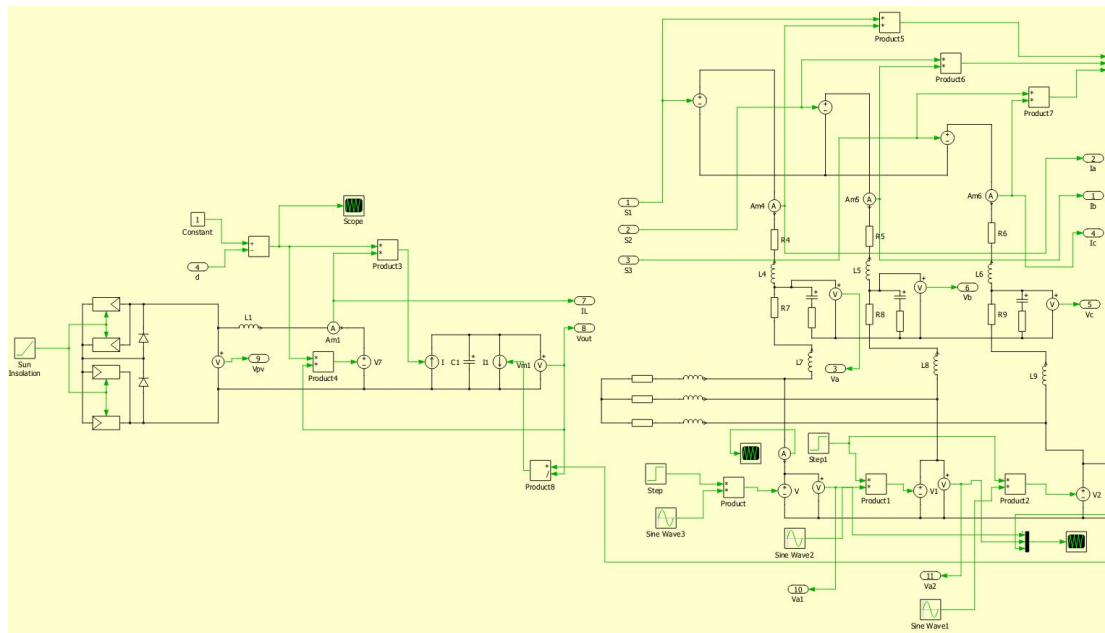

Figure 4.2. Average modeling of complete system in PLECS

circuit of the AC part is the same as the switching model, which involves an LCL filter, the load, and the PCC at which the grid is connected. The voltage magnitude of the controlled

sources are determined from the inverter controller. The realization of the inverter average model is started with a DC source connected at the input of the inverter. Since the DC source has constant voltage, the double loop control used in the switching model will give zero output power, because the outer loop will give zero current reference for the inner loop. Thus, the single loop control method is used. Also, because it is in the modeling stage, only the positive sequence is considered and the negative sequence loop is not designed. The reference for I_d is set to 17 A, and I_q is set to zero. The cross-coupling terms and the feedforward voltage is used that has the similar inner control loop of the switching model. The result is the balanced voltage and current, which confirm the configuration of the inverter design for the final integration of the complete model. The three-phase *abc* voltage is the input voltage for the voltage-controlled source, whereas the switching model has the modulation technique for the gating signal for the inverter switching. The average model of the inverter can be seen in Figure 4.2, which is integrated with the boost converter.

4.3. SIMULATION RESULTS

After completing the individual model designing of the boost converter and the inverter, both the models are integrated as presented in Figure 4.2. The boost controller scheme is the same as the switching model scheme, but the inverter control scheme is changed to the double loop control, which is the same as the switching model. The reason for the inverter control changes now is the need of the DC-link voltage control, which was not required for the constant DC voltage source in the separate design of the inverter control. Also, both the models are linked to each other by connecting a controlled current source parallel with the capacitor. The magnitude of this controlled source is the ratio of the power flow to the output voltage of the boost converter. The complex power is calculated using the capacitor voltage and the inductor current and divided by the DC-link voltage as shown in Figure 4.2. Now, the complete nonlinear average model of the grid-connected PV system is ready for the fault analysis.
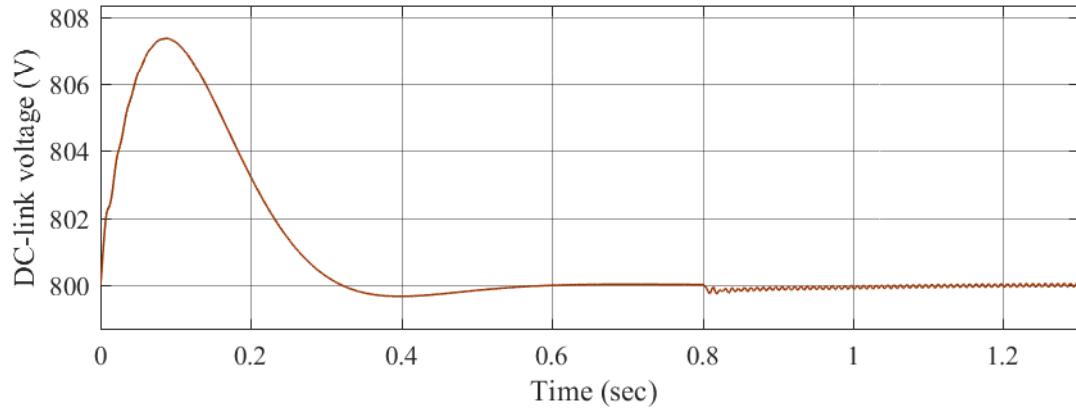
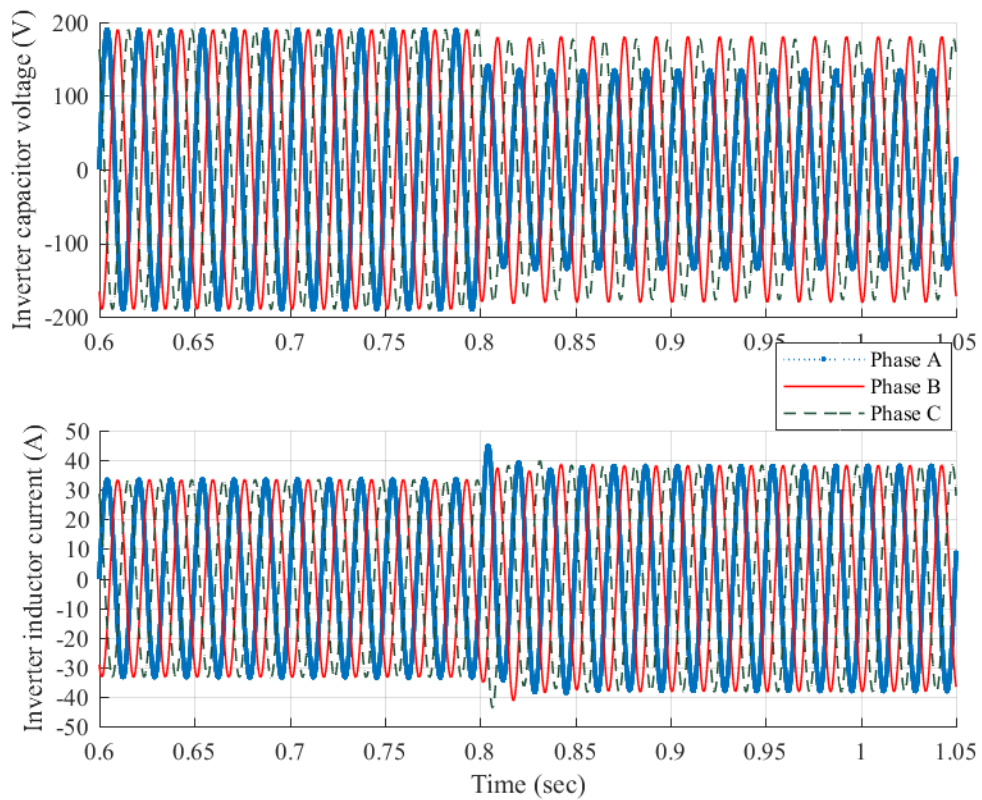Figure 4.3. DC-link voltage during normal and LVRT reactive power injection mode (average model)

Figure 4.4. Inverter capacitor voltage and inductor current during normal and LVRT reactive power injection mode (average model)

The complete average model is run in the MATLAB/PLECS environment for the normal as well as the unbalanced event. An SLG fault having a voltage dip of 0.5 pu is run at t = 0.8 s following the normal operating condition, as shown in Figure 4.3. The inverter control is set to inject the reactive power into the grid. The DC-link voltage oscillations are presented in Figure 4.3, which shows the reduced DC-link voltage oscillations similar to the switching model. The injected current into the grid and the capacitor voltage is presented in
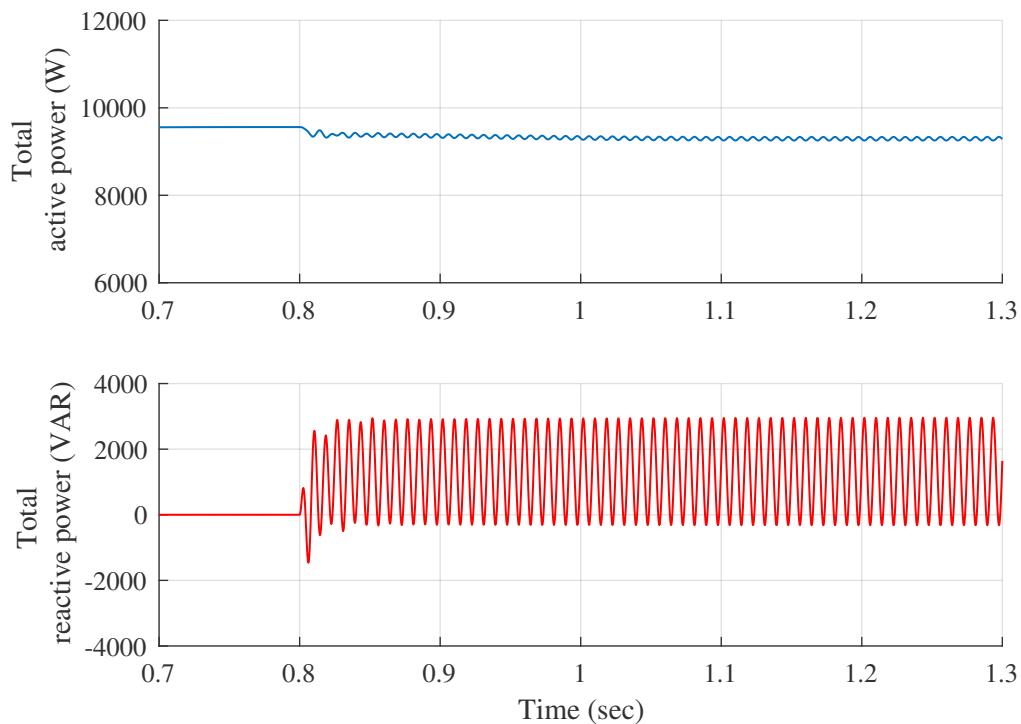

Figure 4.5. Total active and reactive power during LVRT reactive power injection mode (average model)

Figure 4.4, which is nearly same as the switching model results. In addition, the total active and reactive power are presented in Figure 4.5. The total reactive power oscillates due to the double frequency component, which is expected since the control injects the reactive power into the system. The average reactive power is constant, which can be validated from Figure 4.6. The difference between the average and the switching model is the absence of the switching losses in the average model. Thus, the injected current has a slightly higher
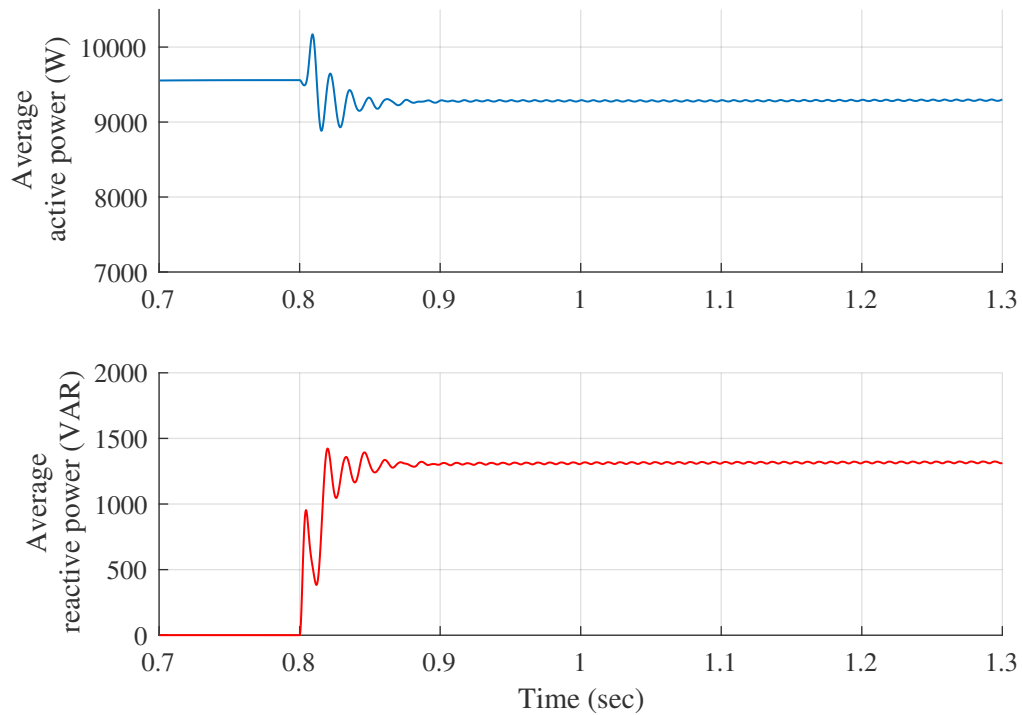
Figure 4.6. Average active and reactive power during LVRT reactive power injection mode (average model)

magnitude of 0.25 A because of the higher power availability compared to the switching model. Other characteristics are very similar to the switching model, and thus, the average model can be used to replace the switching model for the multiple PV grid-connected system.

5. MULTIPLE PV INVERTERS ANALYSIS

The popularity of PV energy production is soaring nowadays, and the penetration of the PV system into the distribution system is increasing. Today, most of the PV generation facilities are scattered and operate in either grid-connected or grid-islanded mode. To reduce the dependence on the grid and improve the overall performance of the system, there will be a need to connect different PV sources to the grid, which will operate in parallel with other connected PVs to the same utility grid. This implies the need for the integration study of multiple PV with the grid during online mode. For multiple PV inverters, the major challenges are power-sharing and the grid-code requirements during the fault events. To observe the performance of the multiple PV inverters in integration with the grid during the fault event, two-inverter modeling is done in the MATLAB/PLECS environment. Next, the fault event is simulated to observe the performance of the inverters during the normal operation and during the fault.

5.1. MODELING OF MULTIPLE PV SYSTEM

The switching model of the three-phase grid-connected system analyzed in the previous sections is deployed here for the multi-inverter grid-connected system. The configuration of the inverters and the grid is shown in Figure 5.1. The line resistance value is 0.01 Ω and the inductance value is 5 mH [22]. Both the inverters have the same set of configuration, as presented in Table 3.4. The power-sharing among the inverters is not designed here because the purpose of the study is the fault analysis. The power generated by both PVs will be delivered to the connected load, and the remaining will flow to the grid. The topology of both systems is similar to the control scheme used for the boost and the inverter. The model presented here represents the interconnection of the PVs, which are separated over certain miles and connected to the utility grid. The individual inverter
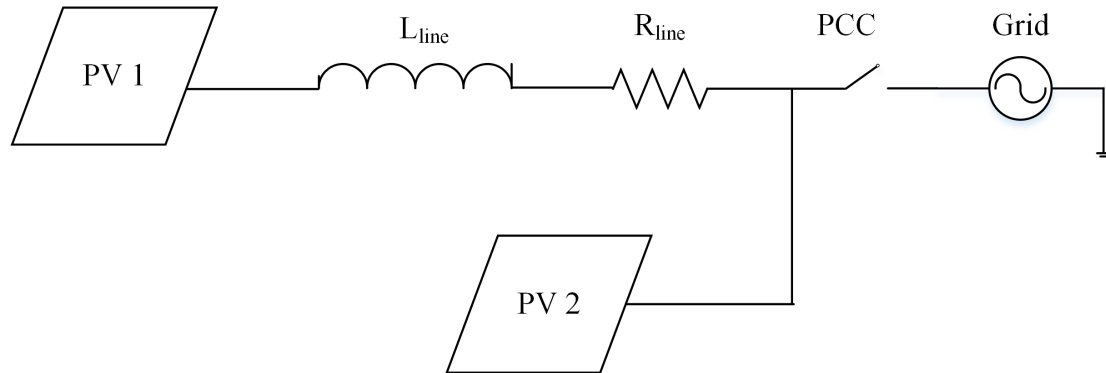
Figure 5.1. Configuration of multiple PV grid-connected system

has a stable operating system during a normal condition as well as during a fault. Next, the fault is initiated at the PCC, which will result in a voltage sag at the PCC. It causes the unbalance voltage condition for both the connected inverters. First, the system is analyzed for the ungrounded system, and then for the grounded system.

5.2. FAULT ANALYSIS OF MULTIPLE PV SYSTEM

Since the topologies of the PV system models are kept the same, the inverters were expected to show the same behavior as the single PV inverter during the normal operating condition and during a fault. The CRG is set to generate the constant average power for both inverters. The fault is initiated at $t = 1$ s. The DC-link voltage behavior for both the inverters is presented in Figure 5.2. It indicates the similar behavior, as expected, and attains the steady state at $t = 0.6$ s. During the fault, it remains constant at 800 V, with the small ripple of tenth of mV. The current profiles for both inverters are similar to previously learned cases of the switching model and the average model and are thus not produced here again. The current attains the nearly balanced nature after the fault for both the inverters, as seen in previous cases. The voltage profile across the capacitor shows the unbalanced nature of the healthy phases of the inverter 1 during the fault. The significant voltage drop of the healthy phase could affect the operation of the sensitive load, which is connected to
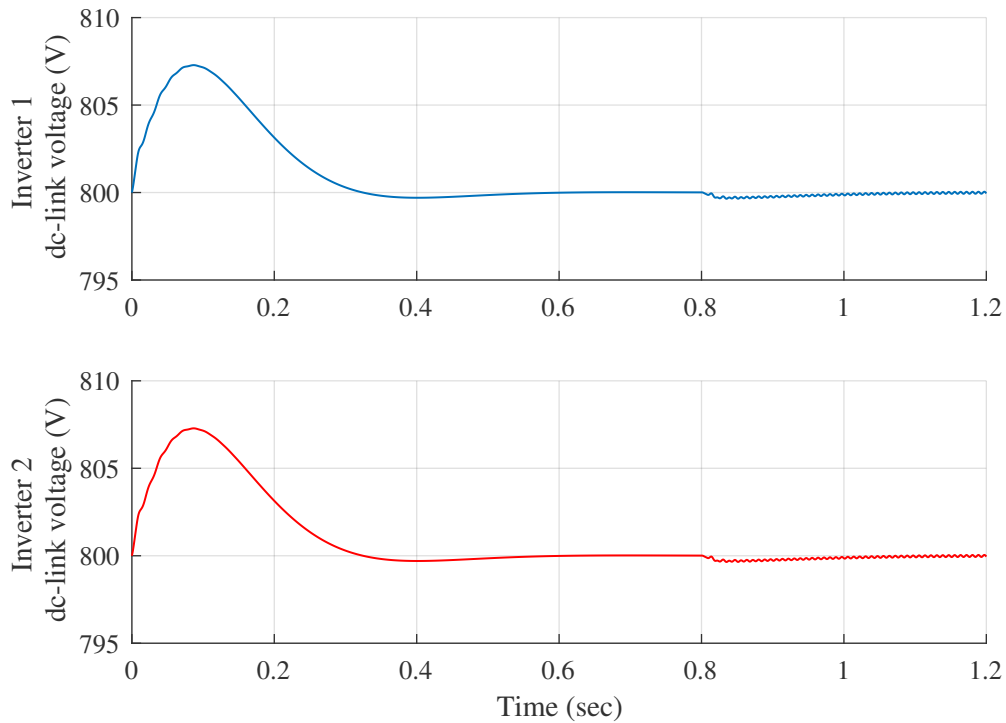
Figure 5.2. DC-link voltages of inverter 1 and 2 during normal and LVRT UPF mode

that phase. The voltage of the healthy phases at the second voltages remains undisturbed, as can be seen in Figure 5.3. The voltage dip occurs for the inverter that has the line impedance in series with it, which is inverter 1 in this study. Inverter 2, which is connected directly to the grid, does not have the voltage unbalance of the healthy phases.

5.3. GROUNDING EFFECT ON FILTER CAPACITOR VOLTAGE

The reason for the voltage dip on the healthy phase is the floating neutral of the capacitor of the LCL filter and the utility grid. Due to the floating neutral, the zero sequence current will not flow from the inverter to the grid. Thus, the zero sequence voltage will be missing for the capacitor voltage. For a wye-connected configuration, the total
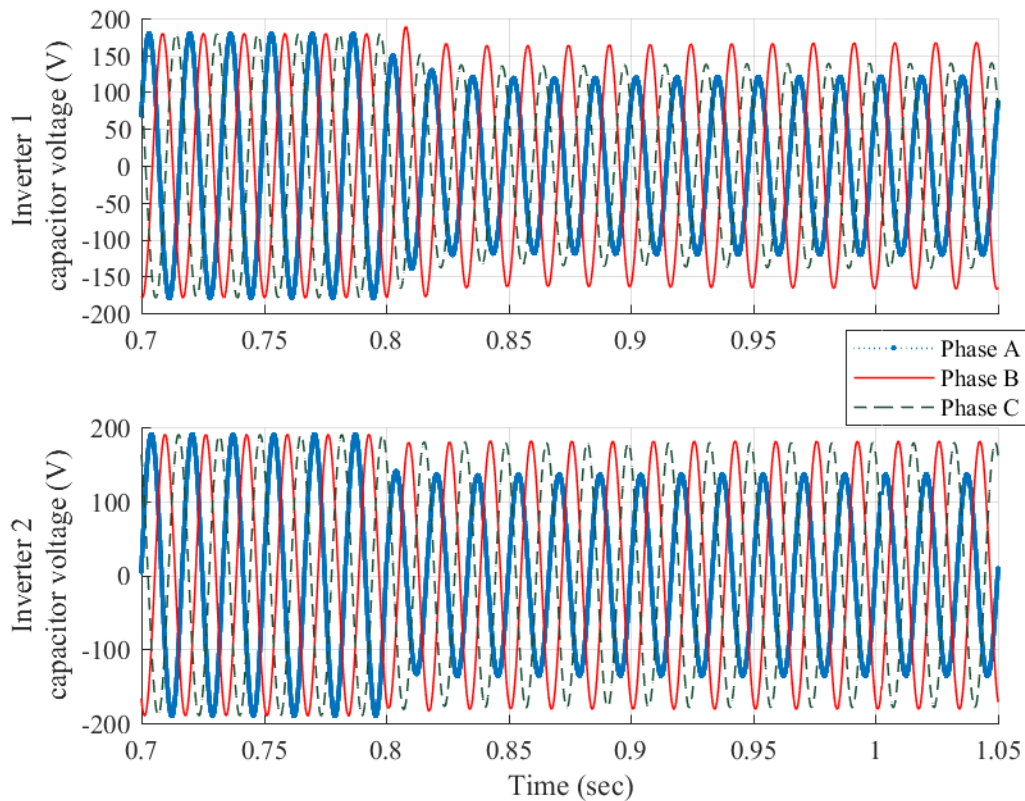
Figure 5.3. Voltage across inverter capacitor 1 and 2 during LVRT UPF mode

voltage of the system can be represented as shown in (5.1)

$$V_{abc} = V_{pos} + V_{neg} + V_{zero} \qquad (5.1)$$

Equation (5.1) indicates the consequences of the absence of the zero sequence voltage on the system voltage. These facts can be observed in Figure 5.4, which represents the voltage across the filter capacitor for the ungrounded system. The absence of the zero sequence voltage affects the healthy phase by causing the voltage dip. It can be observed from the sequence analysis of the inverter voltage from Figure 5.4 that zero sequence voltage is missing. Therefore, the system should be grounded properly in order to include the zero sequence voltage. Thus, the grounding eliminates the voltage dip of the healthy phase as can
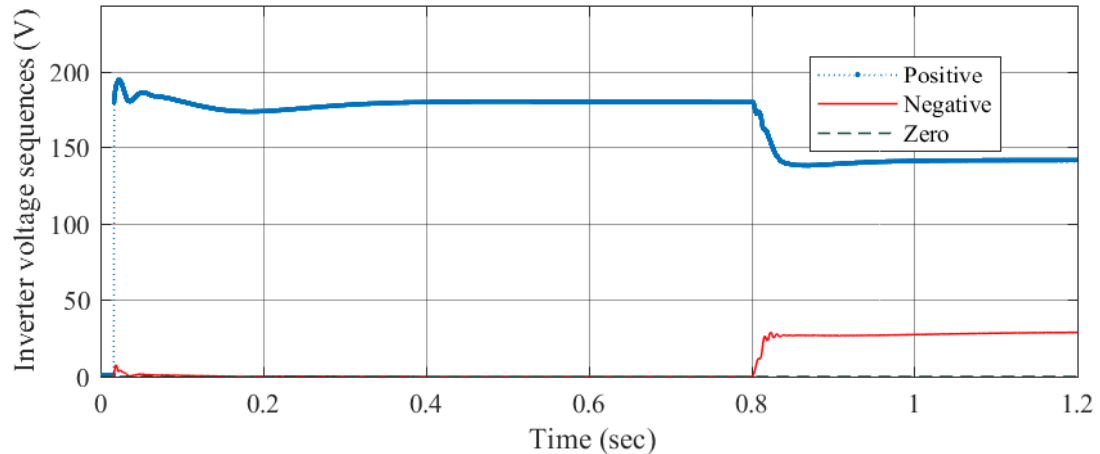
Figure 5.4. Sequence analyzing of inverter 1 voltage without ground
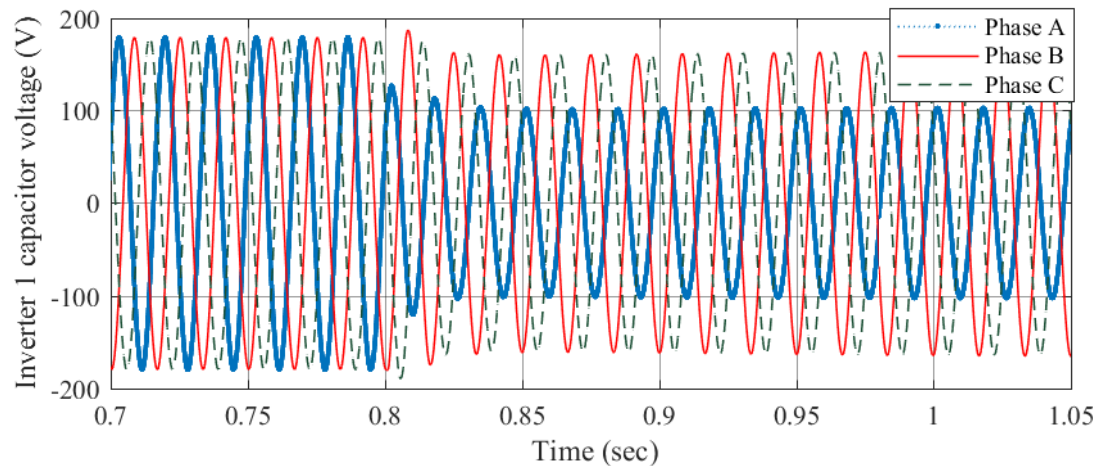
Figure 5.5. Inverter 1 three-phase capacitor voltage with grounding

be seen in Figure 5.5, which represents the three-phase voltage of inverter 1, with grounding in place for the capacitor and the grid-source grounding. Figure 5.6 indicates the presence of the zero sequence voltage during the SLG fault having the grounding in place.

Though grounding was not the major issue for the single PV system, it gets worse for multiple PV systems due to the inclusion of the line impedance in the system. The inclusion of the impedance varies the positive sequence voltage, as can be observed in Figure 5.7.

Figure 5.6. Sequence analyzing of inverter 1 voltage with ground

Thus, the zero sequence component in the system poses an additional burden on the system voltage dip of healthy phase during the fault. Thus, for the single PV array, the system without the grounding does not have the voltage dip on the healthy phase.

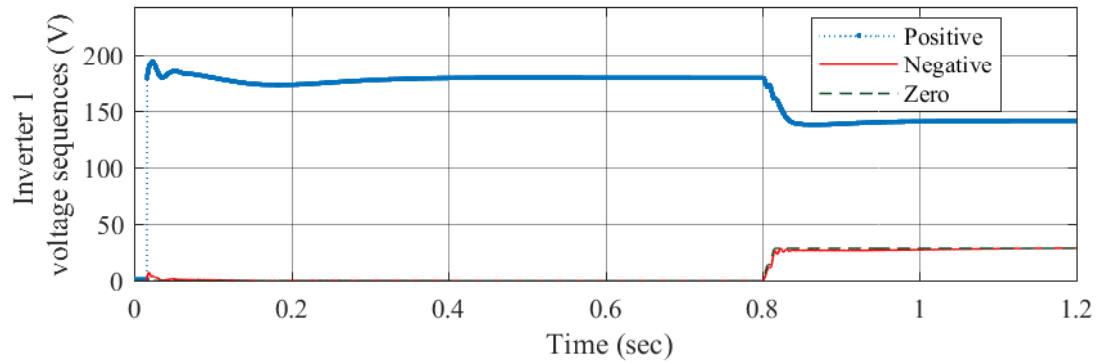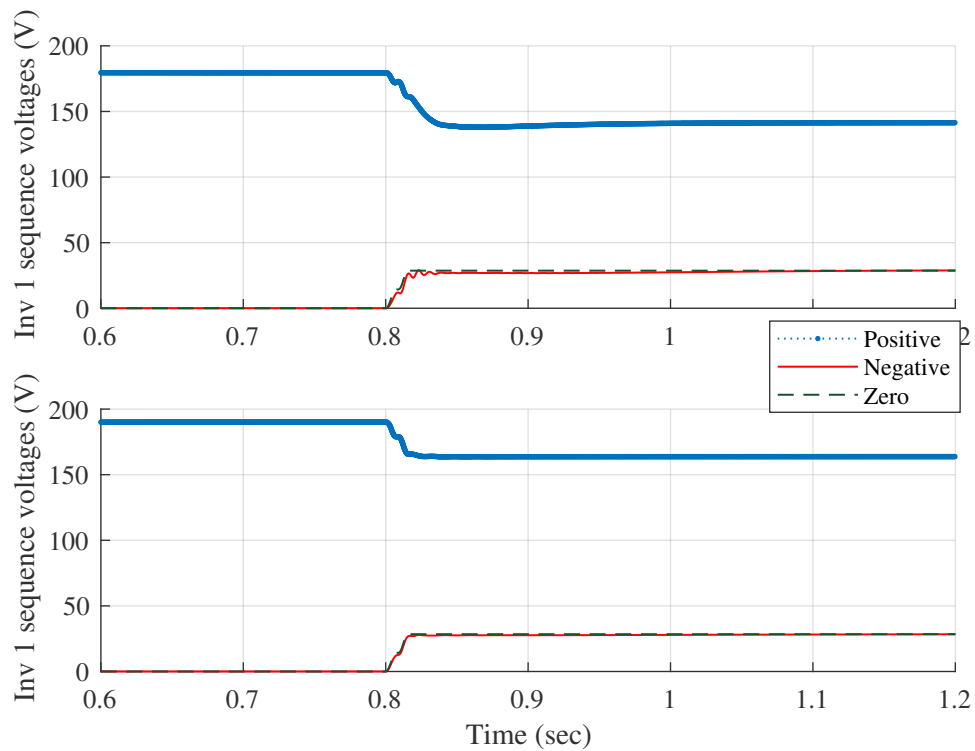Figure 5.7. Sequence comparison of inverter voltage with line inductance (a) 5 mH (b) 1 mH

The comparison of the zero sequence voltage for the line impedance of 1 mH and 5 mH is presented in Figure 5.7. The voltage dip with the higher line inductance would be greater compared to the lower line inductance value for the ungrounded system. Thus, it is important for the multiple PV system to have a firm grounding to avoid any malfunction of the connected loads during faults. The grounding connection should be reviewed thoroughly for the system with higher line impedance.

6. CONCLUSION

The two-stage three-phase grid-connected PV system is studied thoroughly in this work. The complete modeling is presented in steps for the switching model of a single PV system. The importance of the inverter control during LVRT is exploited, considering the future connection requirements. The double loop controller is designed for the boost converter as well as the inverter, and the tuning method is described for both the controllers. The inverter controller is designed using the vector-oriented and feed-forward control. The importance of the positive and negative sequence extraction is explained and it is implemented using the DSOGI method. The complete model is designed in the MATLAB/PLECS environment. The inverter control is designed for the DC-link voltage oscillations elimination and reactive power injection. Both requirements are met using the CRG method. The efficacy is validated by running the SLG fault on the grid during a low voltage event. The designed controller injects the balanced sinusoidal current into the grid during LVRT, and it has some ripple left over due to the presence of a small ripple of double the grid frequency component.

The nonlinear model of the complete PV system is designed for increasing the simulation speed and for the integration study of multiple PV with the grid. The design of an average model of the boost converter and inverter is explained in detail. The results from the average model are validated against the switching model. The multiple PV system is built using the average model of a PV system. The SLG fault is run to simulate the low-voltage event on the grid. The implications of the ungrounded system on the voltage dip of the healthy phase is presented. The sequence analysis is performed for the inverter capacitor voltage for the grounded as well as the ungrounded system. The results indicate

that the voltage dip will be worse for the system that has higher line inductance. Thus, it is important to check the grounding connection to avoid the power quality degradation in a multiple PV system.

The most important contribution of this work is the designing of the switching and the average model of a two-stage three-phase grid-connected PV system. Additionally, it focuses on the CRG process of the inverter control in detail. Lastly, it explains the importance of the grounding for a multiple PV system.

REFERENCES

[1] R. Sabzehgar, "A review of AC/DC microgrid-developments, technologies, and challenges," *2015 IEEE Green Energy and Systems Conference, IGESC 2015*, pp. 11–17, 2015.

[2] A. M. Lede, M. G. Molina, M. Martinez, and P. E. Mercado, "Microgrid architectures for distributed generation: A brief review," *2017 IEEE PES Innovative Smart Grid Technologies Conference - Latin America, ISGT Latin America 2017*, vol. 2017-Janua, pp. 1–6, 2017.

[3] F. Blaabjerg, Z. Chen, and S. B. Kjaer, "Power electronics as efficient interface in dispersed power generation systems," *IEEE Transactions on Power Electronics*, vol. 19, no. 5, pp. 1184–1194, 2004.

[4] F. Blaabjerg, R. Teodorescu, M. Liserre, and A. V. Timbus, "Overview of control and grid synchronization for distributed power generation systems," 2006.

[5] P. Rodríguez, R. Teodorescu, I. Candela, A. V. Timbus, M. Liserre, and F. Blaabjerg, "New positive-sequence voltage detector for grid synchronization of power converters under faulty grid conditions," *PESC Record - IEEE Annual Power Electronics Specialists Conference*, 2006.

[6] E. Storage, *IEEE Standard for Interconnection and Interoperability of Distributed Energy Resources with Associated Electric Power Systems Interfaces Sponsored by the IEEE Standard for Interconnection and Interoperability of Distributed Energy Resources with Associate.* 2018.

[7] P. Rodriguez, a.V. Timbus, R. Teodorescu, M. Liserre, and F. Blaabjerg, "Flexible Active Power Control of Distributed Power Generation Systems During Grid Faults," *IEEE Transactions on Industrial Electronics*, vol. 54, no. 5, pp. 2583–2592, 2007.

[8] H. S. Song and K. Nam, "Dual current control scheme for PWM converter under unbalanced input voltage conditions," *IEEE Transactions on Industrial Electronics*, vol. 46, no. 5, pp. 953–959, 1999.

[9] J. Rocabert, A. Luna, F. Blaabjerg, and I. Paper, "Control of Power Converters in AC Microgrids.pdf," *IEEE Transactions on Power Electronics*, vol. 27, no. 11, pp. 4734–4749, 2012.

[10] J. M. Guerrero, J. C. Vasquez, J. Matas, L. G. De Vicuña, and M. Castilla, "Hierarchical control of droop-controlled AC and DC microgrids - A general approach toward standardization," *IEEE Transactions on Industrial Electronics*, vol. 58, no. 1, pp. 158–172, 2011.

[11] E. Afshari, "A Low-Voltage Ride-Through Control Strategy for Three-Phase Grid-Connected PV Systems," *2017 IEEE Power and Energy Conference at Illinois (PECI)*, no. 1, pp. 1 – 6, 2017.

[12] D. E. Olivares, A. Mehrizi-Sani, A. H. Etemadi, C. A. Cañizares, R. Iravani, M. Kazerani, A. H. Hajimiragha, O. Gomis-Bellmunt, M. Saeedifard, R. Palma-Behnke, G. A. Jiménez-Estévez, and N. D. Hatziargyriou, "Trends in microgrid control," *IEEE Transactions on Smart Grid*, vol. 5, no. 4, pp. 1905–1919, 2014.

[13] M. Villalva, J. Gazoli, and E. Filho, "Comprehensive Approach to Modeling and Simulation of Photovoltaic Arrays," *IEEE Transactions on Power Electronics*, vol. 24, no. 5, pp. 1198–1208, 2009.

[14] D. Beriber and A. Talha, "MPPT techniques for PV systems," *International Conference on Power Engineering, Energy and Electrical Drives*, no. May, pp. 1437–1442, 2013.

[15] N. E. Zakzouk, A. K. Abdelsalam, A. A. Helal, and B. W. Williams, "PV Single-Phase Grid-Connected Converter: DC-Link Voltage Sensorless Prospective," *IEEE Journal of Emerging and Selected Topics in Power Electronics*, vol. 5, no. 1, pp. 526–546, 2017.

[16] T. Huang, X. Shi, Y. Sun, and D. Wang, "Three-phase photovoltaic grid-connected inverter based on feedforward decoupling control," *ICMREE 2013 - Proceedings: 2013 International Conference on Materials for Renewable Energy and Environment*, vol. 2, pp. 476–480, 2013.

[17] J. Guerrero, F. Blaabjerg, T. Zhelev, K. Hemmes, E. Monmasson, S. Jemeï, M. P. Comech, R. Granadino, and J. I. Frau, "Distributed generation: Toward a new energy paradigm," *IEEE Industrial Electronics Magazine*, vol. 4, no. 1, pp. 52–64, 2010.

[18] J. Svensson and A. Sannino, "Improving Voltage Disturbance Rejection for Variable-Speed Wind Turbines," *IEEE Power Engineering Review*, vol. 22, no. 7, p. 53, 2002.

[19] F. Iov, A. D. Hansen, P. Sørensen, and N. A. Cutululis, *Mapping of grid faults and grid codes*, vol. 1617. 2007.

[20] G. J. Kish and P. W. Lehn, "Microgrid design considerations for next generation grid codes," *IEEE Power and Energy Society General Meeting*, pp. 1–8, 2012.

[21] H. Zhao, N. Wu, S. Fan, Y. Gao, L. Liu, Z. Zhao, and X. Liu, "Research on Low Voltage Ride Through Control of PV Grid-connected Inverter Under Unbalance Fault," vol. 86, no. 532.

[22] C. A. Plet, M. Brucoli, J. D. McDonald, and T. C. Green, "Fault models of inverter-interfaced distributed generators: Experimental verification and application to fault analysis," *IEEE Power and Energy Society General Meeting*, pp. 1–8, 2011.

VITA

Paresh Patel was born in Gujarat, India. During his bachelor's study, he worked as an intern at the Bhusawal Thermal Power Station on power generation topics. He also worked as an intern at the Tata Power Receiving Station on a bulk substation operation. He completed his bachelor's in electrical engineering from the Sardar Patel College of Engineering in Mumbai in 2013.After completing his bachelor's, he worked for three years as an electrical procurement engineer in Mumbai, India. He started master's study in electrical engineering at Missouri S&T in 2016. His area of interest is distributed energy resources, microgrid, and power system protection. He received his Master's of Science degree from Missouri S&T in July 2018.